A multi phase-field fracture model for long fiber reinforced composites based on the Puck theory of failure

A. Dean[a,b,*], P.K. Asur Vijaya Kumar[c], J. Reinoso[b], C. Gerendt[a], M. Paggi[c], E. Mahdi[d], R. Rolfes[a]

[a] *Institute of Structural Analysis. Leibniz Universität Hannover, Appelstr. 9A, 30167 Hannover, Germany*
[b] *Elasticity and Strength of Materials Group, School of Engineering, Universidad de Sevilla, Camino de los Descubrimientos s/n, 41092, Seville, Spain*
[c] *IMT School for Advanced Studies Lucca, Piazza San Francesco 19, 55100, Lucca, Italy*
[d] *Department of Mechanical and Industrial Engineering, College of Engineering, Qatar University, P.O. Box 2713, Doha, Qatar*

Abstract

Phase-Field (PF) methods of fracture have emerged as powerful modeling tools for triggering fracture events in solids. These numerical techniques efficiently alleviate mesh dependent pathologies and are very suitable for characterizing brittle as well as quasi-brittle fracture in a wide range of engineering materials and structures including fiber reinforced composites. In this work, a multi phase-field model relying on the Puck's failure theory is proposed for triggering intra-laminar cracking in long fiber reinforced composites. The current formulation encompasses the differentiation of fiber and inter-fiber (matrix-dominated) failure phenomena via the consideration of two independent phase-field damage-like variables, and the corresponding evolution equations and length scales. Moreover, for matrix-dominated deformation states, the present formulations endow the incorporation of plastic effects via an invariant-based plasticity model. Special attention is also devoted to its finite element implementation, which is conducted using the user-defined capabilities `UMAT` and `UEL` of `ABAQUS`, in conjunction with the thorough assessment of its thermodynamic consistency. Several representative applications pinpoint the applicability of the proposed computational tool.

Keywords: A. Fiber Reinforced Composites; B. Fracture Mechanics; C. Finite Element Method (FEM); D. Phase-Field Modeling

The link to the published version of this manuscript is: https://dx.doi.org/10.1016/j.compstruct.2020.112446

1. Introduction

The comprehensive understanding of fracture events in fiber reinforced composites (generally encompassing glass and carbon reinforced polymeric composites, GFRP and CFRP, respectively) is a matter of significant importance in many practical applications, with a strong interest in aerospace and aeronautical industries, widening their applicability to other production sectors. However, under in-service conditions, cracking events generally lead to a drastic reduction of the load-bearing capacity of structural components and the posterior achievement of the corresponding collapsing point.

The complexity of potential failure mechanisms from different signatures in long fiber reinforced composites, i.e. inter-laminar (delamination and decohesion) and intra-laminar (fiber/matrix breakage, fiber kinking, etc), has promoted the development of a range of different predictive models, especially within the context of the Finite Element Method (FEM). In this setting, cohesive-like models have been proven to be an efficient modeling tool for the reliable prediction of delamination events in composite materials and structures at different scales [1, 2, 3, 4, 5, 6]. Focusing on intra-laminar failure, many of the previous

*Corresponding authors
Email address: `a.dean@isd.uni-hannover.de` (A. Dean)

works have exploited the adoption of Continuum Damage Mechanics (CDM)-based formulations in order to account for the distinction between fiber- and matrix-dominated failures relying on the consideration of different internal-like damage variables [7, 8, 9, 10, 11, 12, 13], which can be also applicable to non-local formulations.

In the last decade, the landmark investigation by Francfort and Marigo [14] and its subsequent developments by Bourdin et al. [15, 16], which is denominated as the phase-field approach of fracture, has emerged as a powerful strategy for modeling fracture phenomena in solids and structures via the exploitation and revitalization of the Griffith fracture approach [17, 18, 19]. Phase-Field (PF) methods are characterized by a diffusive crack representation with the prevention of any ad-hoc crack propagation criterion and precluding the implementation of complex crack tracking algorithms [20]. PF models have been validated against theoretical and experimental results [21, 22]. Moreover, the exploitation of these appealing attributes has led to the successful application of PF methods to ductile fracture [18, 23, 24], fatigue, hydrogen-assisted crack failure [25], functionally graded materials, in combination with interface-like crack methods [26, 27], among many other applications.

Within the context of cracking in anisotropic solids, several attempts have been developed so far, see the use of tensor-based anisotropic formulations in anisotropic solids proposed in [28]. Further developments have also concerned the inclusion of anisotropic surface energy which enables capturing complex crack kinking phenomena [29]. One of the most prominent aspects of the intensive development of the PF method in the last decade regarded its modular format which can be applied to non-standard solids regardless of their inherent mechanical response [30, 31], which can also encompass anisotropic elasto-plastic effects [32, 33, 34, 35, 36].

Focusing on modeling failure events in composite materials via PF methods, several approaches have been proposed so far. In this concern, Dal et al. [37, 38], Reinoso et al. [39, 40], Alessi and Freddi [41] and Bleyer and Alessi [42] pinpointed the applicability of PF crack methods to predict damage and failure of composite laminates. Particularly, Bleyer and Alessi [42] derived a multi-field PF formulation that endowed the separate effect of fiber and matrix failure to sing two independent damage-like variables. This pioneering contribution was subsequently revised in [40] via the introduction of a simple phase-field variable with the identification of the most prominent failure mechanisms at the material point level, which is also combined with cohesive-like crack methods in [43, 44]. Notwithstanding, there exists an increasing interest in the development of numerical predictive tools based on the PF method which allows the efficient use of phenomenological failure theories for fiber reinforced composites [13]. Recalling these arguments, the present work concerns with the development of a new PF model for long fiber reinforced composites via the exploitation of the Puck's failure theory [45]. Following the developments presented in [40] and [42], the current investigation introduces the consideration of two independent phase-field crack variables for the distinction between fiber- and matrix-dominated failures. Moreover, the formulation herein proposed endows the definition of two independent length scales for each phase-field variable which can be related with Puck initiation strengths. Finally, non-linear behaviour in shear-dominated response is accounted through elastic–plastic relationships between stress and strain at ply level using an anisotropic invariant-based formulation [34, 46, 47, 48, 49].

The article is organized as follows. The modeling framework is presented in Section 2, and the corresponding variational formulations are outlined in Section 3. Section 4 presents the main aspects for the FE implementation. Subsequently, the model is examined via different representative applications in Section 5. Conclusions of the present investigation are drawn in Section 6.

The article is organized as follows. The modeling framework is presented in Section 2, and the corresponding variational formulations are outlined in Section 3. Section 4 presents the main aspects for the FE implementation. Subsequently, the model is examined via different representative applications in Section 5. Conclusions of the present investigation are drawn in Section 6.

2. Multi phase-field formulation based on the Puck failure theory

In this section, we introduce the fundamental aspects of the current multi phase-field formulation for modeling fracture events in long fiber reinforced composite materials. As stated above, the principal aim

is the construction of a numerical formulation encompassing crack propagation in continuum anisotropic media originated from different physical failure mechanisms.

The current formulation can be derived directly from thermodynamic considerations as proposed in [17], which can be consistently equipped with the variational formalism in the spirit of the phase-field approach of fracture. In this regard, we first formulate the particular form of *total energy density* W per unit volume for anisotropic solids accounting for different failure mechanisms (Section 2.1). Subsequently, the constitutive choices are addressed in Sections 2.2 and 2.3.

2.1. Postulation of the total internal energy density

Restricting our analysis to infinitesimal strains, the point of departure of the current formulation relies on the consideration of an arbitrary body with $\mathcal{B} \in \mathbb{R}^{n_{dim}}$ (n_{dim} is the dimension of the analysis). The delimiting boundary of $\mathcal{B}$ is denoted by $\partial\mathcal{B} \in \mathbb{R}^{n_{dim}-1}$. Throughout the deformation process, the body experiences a displacement field identified by the vector field $\mathbf{u} : \mathcal{B} \rightarrow \mathbb{R}^{n_{dim}}$ at the material point level, hence the infinitesimal strain tensor is defined as follows: $\boldsymbol{\varepsilon} := \nabla^s \mathbf{u}$ with $\boldsymbol{\varepsilon} : \mathcal{B} \rightarrow \mathbb{R}^{n_{dim} \times n_{dim}}$. Prescribed displacement conditions are given by $\mathbf{u} = \overline{\mathbf{u}}$ on $\partial\mathcal{B}_u$, whereas prescribed tractions conditions on the corresponding portion of the boundary are denoted as $\overline{\mathbf{t}} = \boldsymbol{\sigma} \cdot \mathbf{n}$ on $\partial\mathcal{B}_t$ with $\boldsymbol{\sigma}$ identifying the Cauchy stress tensor. Kinematic and static boundary conditions satisfy the standard requirements: $\overline{\partial\mathcal{B}_t \cup \partial\mathcal{B}_u} = \partial\mathcal{B}$ and $\partial\mathcal{B}_t \cap \partial\mathcal{B}_u = \emptyset$, where $\mathbf{n}$ is the external outer normal vector to the body.

In classical continuum damage mechanics (CDM), the total internal energy density is a state function of the deformation tensor $\boldsymbol{\varepsilon}$ and the internal damage-like variable $\mathfrak{d}$ [50]. This basic formulation can be extended to account for non-local effects via the incorporation of the material gradient of $\mathfrak{d}$, i.e. $\nabla\mathfrak{d}$ which allows the circumvention of the ill-posed character of the corresponding Initial Boundary Value Problem (IBVP) upon softening behavior. The consistent generalization of this isotropic damage formulation to account for different failure mechanisms can be postulated by means of recalling an additive decomposition scheme of the *total energy density* W per unit volume, so that it becomes a state function of: (i) the strain field, (ii) the n scalar damage variables $\mathfrak{d}_i$ (with $i = 1, \ldots, n$), and (iii) their respective gradients $\nabla\mathfrak{d}_i$. Based on this decomposition scheme, each individual damage variable is associated with a particular physical failure mechanism and whose evolution is assumed to be confined between 0 (intact state) and 1 (fully broken state). Moreover, as an additional argument of the current formulation, we postulate the evolution of plastic deformation in order to accurately predict the material non-linear behavior under a matrix-dominated response.

With the previous ingredients at hand and advocating the decomposition of the Helmholtz free-energy function proposed by Wagner and Balzani [51], which was successfully exploited in [13] for Puck-based damage model, we assume that the *total energy density* W per unit volume for anisotropic materials can be expressed as follows:

$$W(\boldsymbol{\varepsilon}, \boldsymbol{\varepsilon}^p, \hat{w}^p, \mathfrak{d}_i, \nabla\mathfrak{d}_i, \mathbf{A}) = W_{FF}(\boldsymbol{\varepsilon}, \mathfrak{d}_{FF}, \nabla\mathfrak{d}_{FF}, \mathbf{A}) + W_{IFF}(\boldsymbol{\varepsilon}, \boldsymbol{\varepsilon}^p, \hat{w}^p, \mathfrak{d}_{IFF}, \nabla\mathfrak{d}_{IFF}, \mathbf{A}), \tag{1}$$

where $W_{FF}(\boldsymbol{\varepsilon}, \mathfrak{d}_{FF}, \nabla\mathfrak{d}_{FF}, \mathbf{A})$ and $W_{IFF}(\boldsymbol{\varepsilon}, \boldsymbol{\varepsilon}^p, \hat{w}^p, \mathfrak{d}_{IFF}, \nabla\mathfrak{d}_{IFF}, \mathbf{A})$ correspond to the counterparts associated with the fiber and the inter-fiber failure, respectively, as addressed in Section 2.2. In the previous expression $\mathbf{A}$ identifies a second-order anisotropic tensor which renders: $\hat{\mathbf{A}} = \mathbf{1} + \hat{\alpha}\mathbf{A}$. In this expression, $\mathbf{1}$ denotes the second order identity; $\hat{\alpha}$ stands for a parameter that weights the material direction $\mathbf{a}$, and $\mathbf{A} = \mathbf{a} \otimes \mathbf{a}$.

Note that in the scheme herein proposed, the dissipated energy results from the contribution of each individual failure mechanism which only affects their corresponding counterparts of the elasticity tensor. Therefore, in contrast to Bleyer and Alessi [42], the current constitutive formulation completely precludes the coupling between the different damage variables.

In the forthcoming developments, the total effective Helmholtz free energy function $\hat{\Psi}$ renders:

$$\hat{\Psi}(\boldsymbol{\varepsilon}^e, \mathbf{A}) = \frac{1}{2}\boldsymbol{\varepsilon}^e : \mathbb{C}^e : \boldsymbol{\varepsilon}^e, \tag{2}$$

where $\mathbb{C}^e$ is the elastic constitutive tensor:

$$\mathbb{C}^e := \partial_{\boldsymbol{\varepsilon}^e\boldsymbol{\varepsilon}^e}\hat{\Psi} = \lambda\mathbf{1}\otimes\mathbf{1} + 2\mu_T\mathbb{I} + \alpha(\mathbf{1}\otimes\mathbf{A} + \mathbf{A}\otimes\mathbf{1}) + 2(\mu_L - \mu_T)\mathbb{I}_A + \beta\mathbf{A}\otimes\mathbf{A}, \tag{3}$$

where $\mathbb{I}$ stands for the fourth-order identity matrix; $\mathbb{I}_A = A_{im}\mathbb{I}_{jmkl} + A_{jm}\mathbb{I}_{mikl}$, and λ, α, β, μ_T and μ_L are to the elastic constants:

$$\lambda = E_{22}\left(\nu_{23} + \nu_{31}\nu_{13}\right)/D, \tag{4}$$

$$\alpha = E_{22}\left[\nu_{31}\left(1 + \nu_{32} - \nu_{13}\right) - \nu_{32}\right]/D, \tag{5}$$

$$\beta = E_{11}\left(1 - \nu_{32}\nu_{23}\right)/D - E_{22}\left[1 - \nu_{21}\left(\nu_{12} + 2(1+\nu_{23})\right)\right]/D - 4G_{12}, \tag{6}$$

$$\mu_L = G_{12} \text{ and } \mu_T = G_{23}, \tag{7}$$

with:

$$D = 1 - \nu_{32}^2 - 2\nu_{13}\nu_{31} - 2\nu_{32}\nu_{13}\nu_{31}. \tag{8}$$

Note that usually, 1-direction corresponds to the fiber orientation, 2-direction is transverse in-plane orientation with respect to the fiber direction, and 3-direction stands for transverse out-of-plane orientation.

The specialization of the composing terms of $W(\boldsymbol{\varepsilon}, \boldsymbol{\varepsilon}^p, \hat{w}^p, \mathfrak{d}_i, \nabla\mathfrak{d}_i, \mathbf{A})$ can be established as follows. Starting the derivation with the fiber failure contribution, the corresponding counterpart is given by:

$$W_{FF}(\boldsymbol{\varepsilon}, \mathfrak{d}_{FF}, \nabla\mathfrak{d}_{FF}, \mathbf{A}) = (1 - \mathfrak{d}_{FF})^2\hat{\Psi}^e_{FF}(\boldsymbol{\varepsilon}, \mathbf{A}) + W_{fr,FF}(\mathfrak{d}_{FF}, \nabla\mathfrak{d}_{FF}), \tag{9}$$

with $\hat{\Psi}^e_{FF}$ identifying the elastic contribution associated with the fiber contribution with: $\Psi^e_{FF} = \frac{1}{2}\boldsymbol{\varepsilon} : \mathbb{C}^e_{FF} : \boldsymbol{\varepsilon}$, where:

$$\mathbb{C}^e_{FF} = \begin{bmatrix} \mathbb{C}^e_{11} & 0 & 0 & 0 & 0 & 0 \\ 0 & 0 & 0 & 0 & 0 & 0 \\ 0 & 0 & 0 & 0 & 0 & 0 \\ 0 & 0 & 0 & 0 & 0 & 0 \\ 0 & 0 & 0 & 0 & 0 & 0 \\ 0 & 0 & 0 & 0 & 0 & 0 \end{bmatrix}, \tag{10}$$

and $W_{fr,FF}(\mathfrak{d}_{FF}, \nabla\mathfrak{d}_{FF})$ stands for the inelastic fracture energy due to the fiber breakage, which adopts the form:

$$W_{fr,FF}(\mathfrak{d}_{FF}, \nabla\mathfrak{d}_{FF}) = \mathcal{G}_{c,FF}\left[\gamma(\mathfrak{d}_{FF}, \nabla\mathfrak{d}_{FF})\right] = \mathcal{G}_{c,FF}\left[\frac{1}{2l_{FF}}\mathfrak{d}^2_{FF} + \frac{l_{FF}}{2}|\nabla\mathfrak{d}_{FF}|^2\right]. \tag{11}$$

In the previous expression, $\mathcal{G}_{c,FF}$ identifies as the fracture energy associated with the fiber failure; $\gamma(\mathfrak{d}_{FF}, \nabla\mathfrak{d}_{FF})$ is the crack density functional of this failure mechanism, and l_{FF} is the characteristic length scale in the phase-field approach of fracture associated with fiber failure. According to [22], the length scale parameter can be related to the apparent material strength as follows:

$$l_{FF} = \frac{27}{256}\frac{E_{11}\mathcal{G}_{c,FF}}{\sigma^2_{s,FF}}, \tag{12}$$

where $\sigma_{s,FF}$ is the material strength associated with fiber failure.

Similarly, the inter-fiber failure contribution (also accounting for the plastic deformation) can be expressed as:

$$W_{IFF}(\boldsymbol{\varepsilon}, \boldsymbol{\varepsilon}^p, \hat{w}^p, \mathfrak{d}_{IFF}, \nabla\mathfrak{d}_{IFF}, \mathbf{A}) = (1-\mathfrak{d}_{IFF})^2\hat{\Psi}^e_{IFF}(\boldsymbol{\varepsilon}-\boldsymbol{\varepsilon}^p, \mathbf{A}) + \Psi^p(\hat{w}^p, \mathfrak{d}_{IFF}, \mathbf{A}) + W_{fr,IFF}(\mathfrak{d}_{IFF}, \nabla\mathfrak{d}_{IFF}), \tag{13}$$

where,

- $\hat{\Psi}^e_{IFF}$ is the elastic-contribution associated with the matrix response: $\hat{\Psi}^e_{IFF} = \frac{1}{2}\boldsymbol{\varepsilon}^e : \mathbb{C}^e_{IFF} : \boldsymbol{\varepsilon}^e$, and:

$$\mathbb{C}^e_{IFF} = \begin{bmatrix} 0 & \mathbb{C}^e_{12} & \mathbb{C}^e_{13} & 0 & 0 & 0 \\ \mathbb{C}^e_{21} & \mathbb{C}^e_{22} & \mathbb{C}^e_{23} & 0 & 0 & 0 \\ \mathbb{C}^e_{31} & \mathbb{C}^e_{32} & \mathbb{C}^e_{33} & 0 & 0 & 0 \\ 0 & 0 & 0 & \mathbb{C}^e_{44} & 0 & 0 \\ 0 & 0 & 0 & 0 & \mathbb{C}^e_{55} & 0 \\ 0 & 0 & 0 & 0 & 0 & \mathbb{C}^e_{66} \end{bmatrix}. \tag{14}$$

- $\Psi^p(\hat{w}^p, \mathfrak{d}_{IFF}, \mathbf{A})$ stands for energy contribution associated with plastic deformation, whose particular expression is given by:

$$\Psi^p(\hat{w}^p, \mathfrak{d}_{IFF}, \mathbf{A}) = (1-\mathfrak{d}_{IFF})^2 \hat{w}^p(\boldsymbol{\varepsilon}^p, \mathbf{A}) \text{ with } \hat{w}^p = \int_0^t \hat{\phi}(\dot{\varepsilon}^p, \mathbf{A})\, \mathrm{d}t', \tag{15}$$

with $\hat{\phi}(\dot{\varepsilon}^p, \mathbf{A})$ is the effective plastic dissipation potential as a function of the temporal derivative of the plastic deformation for the elapsed time t throughout the deformation process. Moreover, note that without any loss of generality, we adopt the same degradation function for the elastic and plastic contributions in the part of the energy associated with inter-fiber failure.

- Finally, $W_{fr,IFF}(\mathfrak{d}_{IFF}, \nabla\mathfrak{d}_{IFF})$ is the dissipated energy due to matrix failure, and whose particular form is given by:

$$W_{fr,IFF}(\mathfrak{d}_{IFF}, \nabla\mathfrak{d}_{IFF}) = \mathcal{G}_{c,IFF}\left[\gamma(\mathfrak{d}_{IFF}, \nabla\mathfrak{d}_{IFF})\right] = \mathcal{G}_{c,IFF}\left[\frac{1}{2l_{IFF}}\mathfrak{d}^2_{IFF} + \frac{l_{IFF}}{2}|\nabla\mathfrak{d}_{IFF}|^2\right]. \tag{16}$$

where $\mathcal{G}_{c,IFF}$ is the fracture energy corresponding to matrix failure, and l_{IFF} is the corresponding length scale. Similarly, the length scale parameter is estimated as:

$$l_{IFF} = \frac{27}{256}\frac{E_{22}\mathcal{G}_{c,IFF}}{\sigma^2_{s,IFF}}, \tag{17}$$

where $\sigma_{s,IFF}$ is the material strength associated with inter-fiber failure, i.e. matrix cracking.

Note that with the previous definitions at hand, the damaged constitutive stiffness reads:

$$\mathbb{C}(\mathfrak{d}_{FF}, \mathfrak{d}_{IFF}) = (1-\mathfrak{d}_{FF})^2\mathbb{C}^e_{FF} + (1-\mathfrak{d}_{IFF})^2\mathbb{C}^e_{IFF}, \tag{18}$$

$$\mathbb{C}(\mathfrak{d}_{FF}, \mathfrak{d}_{IFF}) = \begin{bmatrix} \mathcal{P}_1\mathbb{C}^e_{11} & \mathcal{P}_2\mathbb{C}^e_{12} & \mathcal{P}_2\mathbb{C}^e_{13} & 0 & 0 & 0 \\ \mathcal{P}_2\mathbb{C}^e_{21} & \mathcal{P}_2\mathbb{C}^e_{22} & \mathcal{P}_2\mathbb{C}^e_{23} & 0 & 0 & 0 \\ \mathcal{P}_2\mathbb{C}^e_{31} & \mathcal{P}_2\mathbb{C}^e_{32} & \mathcal{P}_2\mathbb{C}^e_{33} & 0 & 0 & 0 \\ 0 & 0 & 0 & \mathcal{P}_{12}\mathbb{C}^e_{44} & 0 & 0 \\ 0 & 0 & 0 & 0 & \mathcal{P}_{12}\mathbb{C}^e_{55} & 0 \\ 0 & 0 & 0 & 0 & 0 & \mathcal{P}_2\mathbb{C}^e_{66} \end{bmatrix}, \tag{19}$$

where $\mathcal{P}_1 = (1-\mathfrak{d}_{FF})^2$, $\mathcal{P}_2 = (1-\mathfrak{d}_{IFF})^2$, and $\mathcal{P}_{12} = \min(\mathcal{P}_1, \mathcal{P}_2)$.

As final comments, it is worth to remark that: (i) the current damage-based evolutions for fiber and inter-fiber failures recall the quadratic dissipation function within the context of the phase-field approach of fracture. Further extensions of the proposed formulation can be made using the so-called PF-CZM for homogeneous media proposed by Wu and co-authors [52], which is a matter beyond the scope of the present investigation. (ii) The current formulation is equipped with two different length scales, l_{FF} and l_{IFF}, which are associated with different intra-laminar failure mechanisms and are linked with the respective fracture energies $\mathcal{G}_{c,FF}$ and $\mathcal{G}_{c,IFF}$. Moreover, such length scales are recalled as numerical regularizing parameters since the damage initiation is triggered upon the evaluation of the Puck failure criteria (Section 2.2).

2.2. Phenomenological failure criterion: fundamentals of the Puck failure theory

The condition of damage evolution at the material point level relies on the assessment of the Puck failure criteria [53, 45], which distinguish between two main failure mechanisms: (i) fiber failure and (ii) inter-fiber failure (matrix-dominated cracking). The ply coordinates are expressed in the local setting $0-\mathbf{e}_1-\mathbf{e}_2-\mathbf{e}_3$, see Figure 1.a. As customary, the fiber direction corresponds to the symbol $\parallel$ (subscript 1), whilst the directions transverse to the fiber direction in-plane (subscript 2) and out-of-plane (subscript 3) are denoted by the symbol $\perp$.

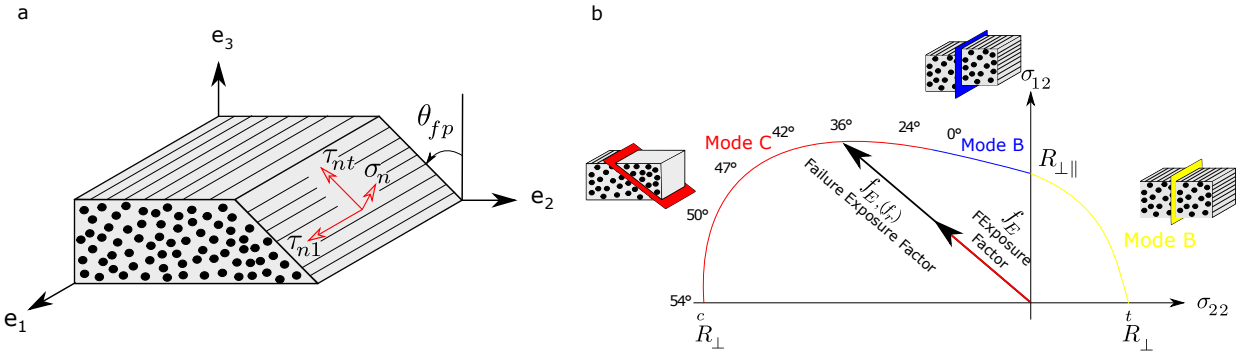

Figure 1: Puck failure theory: (a) action plane concept and the definition of acting stresses (stressing) on the fracture plane whose angle is denoted by Θ_{fp} and (b) visualization of the exposure factor f_E and the exposure factor at the failure point $f_{E,fr}$ [53].

According to Puck's theory, fiber failure is attained through the violation of the corresponding failure criterion in tension and compressions.

In this setting, for each of the identified failure mechanisms, fracture can be triggered by the evaluation of the corresponding failure exposure factors (material efforts) that relate the length of a pseudo vector $\boldsymbol{\varpi}$ and that corresponding to the fracture vector $\boldsymbol{\varpi}_{fr}$, i.e. $f_E = |\boldsymbol{\varpi}| \,/\, |\boldsymbol{\varpi}_{fr}|$, see [53]. Therefore, failure is initiated when the exposure factor f_E reaches 1, whereas subsequent failure progression relies on energetic considerations inline with standard PF methods of fracture.

The exposure factor for fiber failure under tensile stress conditions, which is denoted by the subscript $FF+$, is given by:

$$f_{E,FF+} = \frac{1}{R^t_{\parallel}} \left[\bar{\sigma}_{11} - \left(\nu_{\perp\parallel} - \frac{E_{\parallel}}{E_{\parallel f}} \nu_{\perp\parallel f} \right) \left(\bar{\sigma}_{22} + \bar{\sigma}_{33} \right) \mathcal{P}_2 \right], \tag{20}$$

where $R^t_{\parallel}$ stands for the tensile longitudinal strength in fiber direction. $\nu_{\perp\parallel}$ and $\nu_{\perp\parallel f}$ identify the major Poisson's ratios of the ply and the fibers, respectively, and $E_{\parallel f}$ is the elastic modulus of the fibers.

The exposure factor for fiber failure in compression reads:

$$f_{E,FF-} = \sqrt{\left(\frac{1}{R^c_{\parallel}} \left[\bar{\sigma}_{11} - \left(\nu_{\perp\parallel} - \frac{E_{\parallel}}{E_{\parallel f}} \nu_{\perp\parallel f} m_{\sigma f} \right) \mathcal{P}_2 \left(\bar{\sigma}_{22} + \bar{\sigma}_{33} \right) \right] \right)^2 + \kappa \left(\frac{\bar{\sigma}^2_{12} + \bar{\sigma}^2_{13}}{R^2_{\perp\parallel}} \right)}, \tag{21}$$

where $R^c_{\parallel}$ is the compressive longitudinal strength in fiber direction, $R_{\perp\parallel}$ represents the in-plane shear strength, and $m_{\sigma f}$ stands for the so-called magnification factor, which is assumed to take the values 1.1 for CFRP and 1.3 for GFRP [53]. The incorporation of $\mathcal{P}_2$ is to scale the influence of the transverse stress components on the longitudinal stress (lateral contraction) with respect to the state of matrix damage. It is assumed that the contraction in the longitudinal direction due to transverse stress will vanish in a case $\mathcal{P}_2 \to 1$, i.e. matrix rupture parallel to the fibers. In the case of compressive longitudinal stress, reduced compressive longitudinal fracture resistance of the plies is assumed in case of increasing shear stress. The parameter κ allows controlling the influence of shear stresses on the failure of the fibers under compression.

In the case of lateral constraint $\kappa = 0$, because even in case of a crushed matrix the fibers are assumed to be kept in line by the lateral constraint. In case of absent lateral constrains $\kappa \geq 0$, since a crushed matrix will promote fiber kinking and will, therefore, reduce the compressive load capacities in fiber direction.

With regard to the inter-fiber failure, Puck theory introduced the concept of the so-called fracture plane [53, 45], and hence the inter-fiber failure criterion is based on the identification of the fracture angle θ_{fp} and fracture plane with the highest exposure factor $F_{E,IFF}$. The determination of the fracture plane is usually performed via the assessment of the most critical stress state in terms of the local components by calculating the value of $F_{E,IFF}$ for all angles θ within the interval of $-90° \leq \theta \leq +90°$, using an increment of one degree. The transformation from the local ply setting to the action plane system yields:

$$\begin{bmatrix} \bar{\sigma}_n(\theta) \\ \bar{\tau}_{nt}(\theta) \\ \bar{\tau}_{n1}(\theta) \end{bmatrix} = \begin{bmatrix} \cos^2\theta & \sin^2\theta & 2\cos\theta\sin\theta & 0 & 0 \\ -\cos\theta\sin\theta & \cos\theta\sin\theta & \cos^2\theta - \sin^2\theta & 0 & 0 \\ 0 & 0 & 0 & \sin\theta & \cos\theta \end{bmatrix} \begin{bmatrix} \bar{\sigma}_{22} \\ \bar{\sigma}_{33} \\ \bar{\sigma}_{23} \\ \bar{\sigma}_{13} \\ \bar{\sigma}_{12} \end{bmatrix}. \tag{22}$$

The particular expressions for inter-fiber failure under tensile and compressive loading conditions on the action plane are given by the following, respectively:

$$f_{E,IFF+}(\theta) = \begin{cases} \left[\sqrt{\left[\left(\frac{1}{R_{\perp}^{At}} - \frac{p_{\perp\psi}^{t}}{R_{\perp\psi}^{A}} \right) \bar{\sigma}_n(\theta) \right]^2 + \left(\frac{\bar{\tau}_{nt}(\theta)}{R_{\perp\perp}^{A}} \right)^2 + \left(\frac{\bar{\tau}_{n1}(\theta)}{R_{\parallel\perp}^{A}} \right)^2} + \frac{p_{\perp\psi}^{t}}{R_{\perp\psi}^{A}} \bar{\sigma}_n(\theta) \right] \\ \frac{1}{\eta_w} \text{ for } \bar{\sigma}_n(\theta) \geq 0, \end{cases} \tag{23}$$

$$f_{E,IFF-}(\theta) = \begin{cases} \left[\sqrt{\left(\frac{p_{\perp\psi}^{c}}{R_{\perp\psi}^{A}} \bar{\sigma}_n(\theta) \right)^2 + \left(\frac{\bar{\tau}_{nt}(\theta)}{R_{\perp\perp}^{A}} \right)^2 + \left(\frac{\bar{\tau}_{n1}(\theta)}{R_{\parallel\perp}^{A}} \right)^2} + \frac{p_{\perp\psi}^{c}}{R_{\perp\psi}^{A}} \bar{\sigma}_n(\theta) \right] \\ \frac{1}{\eta_w} \text{ for } \bar{\sigma}_n(\theta) < 0, \end{cases} \tag{24}$$

In the previous expressions, η_w accounts for the influence of the exposure factor in fiber direction on the inter-fiber failure due to lateral contraction, as long as no fiber failure occurred. Moreover, one can identify $R_{\perp}^{At} = R_{\perp}^{t}$, $R_{\perp\parallel}^{A} = R_{\perp\parallel}$, where $R_{\perp}^{t}$ represents the transverse tensile strength. Also, the fracture strength $R_{\perp\perp}^{A}$ is given by:

$$R_{\perp\perp}^{A} = \frac{R_{\perp}^{c}}{2\left(1 + p_{\perp\perp}^{c}\right)}, \tag{25}$$

where $R_{\perp}^{c}$ represents the transverse compressive strength of the ply. The definitions of the inclination parameters $p_{\perp\psi}^{t}$ and $p_{\perp\psi}^{c}$ at any angle ψ are given by the following relations, respectively:

$$\frac{p_{\perp\psi}^{t}}{R_{\perp\psi}^{A}} = \frac{p_{\perp\perp}^{t}}{R_{\perp\perp}^{A}} \cos^2\psi + \frac{p_{\perp\parallel}^{t}}{R_{\perp\parallel}^{A}} \sin^2\psi \text{ and } \frac{p_{\perp\psi}^{c}}{R_{\perp\psi}^{A}} = \frac{p_{\perp\perp}^{c}}{R_{\perp\perp}^{A}} \cos^2\psi + \frac{p^{c}\perp\parallel}{R_{\perp\parallel}^{A}} \sin^2\psi, \tag{26}$$

with:

$$R_{\perp\psi}^{A} = \left[\left(\frac{\cos\psi}{R_{\perp\perp}^{A}} \right)^2 + \left(\frac{\sin\psi}{R_{\perp\parallel}^{A}} \right)^2 \right]. \tag{27}$$

The trigonometric terms defined as:

$$\cos^2\psi = \frac{\bar{\tau}_{nt}^2}{\bar{\tau}_{nt}^2 + \bar{\tau}_{n1}^2} \text{ and } \sin^2\psi = \frac{\bar{\tau}_{n1}^2}{\bar{\tau}_{nt}^2 + \bar{\tau}_{n1}^2}. \tag{28}$$

Finally, recommended values of material-dependent inclination parameters $p^t_{\perp\perp}$, $p^c_{\perp\perp}$, $p^t_{\perp\parallel}$, and $p^c_{\perp\parallel}$ are reported in Table 1 for glass fiber reinforced (GFRP) and carbon fiber reinforced (CFRP) composites.

Material	$p^t_{\perp\perp}$	$p^c_{\perp\perp}$	$p^t_{\perp\parallel}$	$p^c_{\perp\parallel}$
GFRP	0.30	0.25	0.20	0.25
CFRP	0.35	0.30	0.25	0.30

Table 1: Recommended inclination factors for CFRP and GFRP composites

2.3. Plasticity formulation for matrix-dominated response

The present section introduces an anisotropic plasticity model for the characterization of matrix-dominated response in long fiber reinforced composites [32, 33, 34]. Via standard plasticity arguments, the total strain tensor $\boldsymbol{\varepsilon}$ can be additively decomposed into elastic $\boldsymbol{\varepsilon}^e$ and plastic $\boldsymbol{\varepsilon}^p$ counterparts:

$$\boldsymbol{\varepsilon} = \boldsymbol{\varepsilon}^e + \boldsymbol{\varepsilon}^p. \tag{29}$$

The effective potential energy precluding fracture events $\hat{\Psi}$ can be expressed as:

$$\hat{\Psi}(\boldsymbol{\varepsilon}^e, \mathbf{A}, \hat{w}^p) = \hat{\Psi}^e(\boldsymbol{\varepsilon}^e, \mathbf{A}) + \hat{\Psi}^p(\hat{w}^p). \tag{30}$$

with:

$$\hat{\Psi}^e(\boldsymbol{\varepsilon}^e, \mathbf{A}) = \frac{1}{2}\boldsymbol{\varepsilon}^e : \mathbb{C}^e : \boldsymbol{\varepsilon}^e, \tag{31}$$

and $\mathbb{C}^e$ denoting the elastic tensor introduced above.

Correspondingly, the elastic domain $\mathbb{E}$ can be expressed as:

$$\mathbb{E} = \{(\bar{\varepsilon}^p) \mid f(\hat{\boldsymbol{\sigma}}, \mathbf{A}, \bar{\varepsilon}^p) \leq 0\}, \tag{32}$$

where $\bar{\varepsilon}^p$ is the equivalent plastic strain: $\bar{\varepsilon}^p = \sqrt{\frac{1}{2}}\|\boldsymbol{\varepsilon}^p\|$. The particular form of the yield function $\mathcal{F}(\hat{\boldsymbol{\sigma}}, \mathbf{A}, \bar{\varepsilon}^p)$ is given by:

$$\mathcal{F}(\hat{\boldsymbol{\sigma}}, \mathbf{A}, \bar{\varepsilon}^p) = \zeta_1 I_1 + \zeta_2 I_2 + \zeta_3 I_3 + \zeta_4 I_3^2 - 1 \leq 0, \tag{33}$$

where I_i $(i = 1, 3)$ identify to the family of the stress invariants representing the integrity basis and whose expressions are omitted here for the sake of brevity, see [32, 33] for further details.

In Eq.(33), the yielding parameters are identified by: $\zeta_i(\bar{\varepsilon}^p)$ $(i = 1, 4)$ which represent different loading states and can be characterized via experimental procedures.

The adoption of a pressure-dependent response is retrieved through the use of a non-associative flow rule inline with [32, 33, 34]. This plastic response is characterized by an invariant-based pressure-dependent quadratic transversely isotropic plastic potential function $\mathcal{G}(\hat{\boldsymbol{\sigma}}, \mathbf{A})$, whose definition is expressed as follows:

$$\mathcal{G}(\hat{\boldsymbol{\sigma}}, \mathbf{A}) = \varsigma_1 I_1 + \varsigma_2 I_2 + \varsigma_3 I_3^2 - 1, \tag{34}$$

where ς_i $(i = 1, 3)$ denotes the plastic potential parameters.

Finally, the maximum energy dissipation principle is exploited for the definition of the evolution equations for the plastic rate of deformation. Such evolution equations are expressed in terms of the internal variables of the model, i.e. the plastic strains $\boldsymbol{\varepsilon}^p$ as follows:

$$\dot{\boldsymbol{\varepsilon}}^p = \gamma^p \frac{\partial \mathcal{G}(\hat{\boldsymbol{\sigma}}, \mathbf{A})}{\partial \hat{\boldsymbol{\sigma}}}, \tag{35}$$

where γ is the so-called plastic multiplier.

With these derivations at hand, the Kuhn-Tucker (KT) loading/unloading conditions can be expressed as:

$$\gamma^p \geq 0,\ \mathcal{F}(\hat{\boldsymbol{\sigma}}, \mathbf{A}, \bar{\varepsilon}^p) \leq 0 \text{ and } \gamma^p \mathcal{F}(\hat{\boldsymbol{\sigma}}, \mathbf{A}, \bar{\varepsilon}^p) = 0, \tag{36}$$

whilst the consistency condition reads:

$$\gamma^p \dot{\mathcal{F}}(\hat{\boldsymbol{\sigma}}, \mathbf{A}, \bar{\varepsilon}^p) = 0. \tag{37}$$

3. Variational formulation and thermodynamics aspects

In the sequel, the variational formulation of the present model is derived, see [54] for more comprehensive details. The total energy functional of the body, $\Pi(\mathbf{u}, \mathfrak{d}_i)$ at an arbitrary instant t, can be formulated as:

$$\Pi(\mathbf{u}, \mathfrak{d}_i) = \Pi_{int}(\mathbf{u}, \mathfrak{d}_i) + \Pi_{ext}(\mathbf{u}), \tag{38}$$

where $\Pi_{int}(\mathbf{u}, \mathfrak{d})$ and $\Pi_{ext}(\mathbf{u})$ are the internal and external contribution to the energy functional, respectively:

$$\Pi_{int}(\mathbf{u}, \mathfrak{d}_i) = \int_{\mathcal{B}} W(\boldsymbol{\varepsilon}, \boldsymbol{\varepsilon}^p, \hat{w}^p, \mathfrak{d}_i, \nabla \mathfrak{d}_i, \mathbf{A}) \mathrm{d}\mathcal{B} = \Pi_{int,FF}(\mathbf{u}, \mathfrak{d}_{FF}) + \Pi_{int,IFF}(\mathbf{u}, \mathfrak{d}_{IFF}), \tag{39}$$

$$\Pi_{ext}(\mathbf{u}) = -\int_{\mathcal{B}} \mathbf{f}_v \mathrm{d}\mathcal{B} - \int_{\partial \mathcal{B}_t} \bar{\mathbf{t}} \mathrm{d}\partial\mathcal{B}, \tag{40}$$

where $\mathbf{f}_v$ is the deformation-independent volume-specific loads and:

$$\begin{aligned} \Pi_{int,FF}(\mathbf{u}, \mathfrak{d}_{FF}) &= \int_{\mathcal{B}} W_{FF}(\boldsymbol{\varepsilon}, \mathfrak{d}_{FF}, \nabla \mathfrak{d}_{FF}, \mathbf{A}) \mathrm{d}\mathcal{B} \\ &= \int_{\mathcal{B}} (1 - \mathfrak{d}_{FF})^2 \hat{\Psi}^e_{FF}(\boldsymbol{\varepsilon}, \mathbf{A}) \mathrm{d}\mathcal{B} + \int_{\mathcal{B}} \mathcal{G}_{c,FF} \left[\frac{1}{2 l_{FF}} \mathfrak{d}^2_{FF} + \frac{l_{FF}}{2} |\nabla \mathfrak{d}_{FF}|^2 \right] \mathrm{d}\mathcal{B}, \end{aligned} \tag{41}$$

$$\begin{aligned} \Pi_{int,IFF}(\mathbf{u}, \mathfrak{d}_{IFF}) &= \int_{\mathcal{B}} W_{IFF}(\boldsymbol{\varepsilon} - \boldsymbol{\varepsilon}^p, \mathfrak{d}_{IFF}, \nabla \mathfrak{d}_{IFF}, \mathbf{A}) \mathrm{d}\mathcal{B} \\ &= \int_{\mathcal{B}} (1 - \mathfrak{d}_{IFF})^2 \hat{\Psi}^e_{IFF}(\boldsymbol{\varepsilon} - \boldsymbol{\varepsilon}^p, \mathbf{A}) \mathrm{d}\mathcal{B} + \int_{\mathcal{B}} \Psi^p(\hat{w}^p, \mathfrak{d}_{IFF}) \mathrm{d}\mathcal{B} \\ &+ \int_{\mathcal{B}} \mathcal{G}_{c,IFF} \left[\frac{1}{2 l_{IFF}} \mathfrak{d}^2_{IFF} + \frac{l_{IFF}}{2} |\nabla \mathfrak{d}_{IFF}|^2 \right] \mathrm{d}\mathcal{B}. \end{aligned} \tag{42}$$

Recalling the standard Bubnov-Galerkin method, the three primary fields with:

$$\mathbf{u} \in \mathcal{U}_u := \left\{ \mathbf{u} \in H^1(\mathcal{B}) | \nabla \mathbf{u} \in L^2(\mathcal{B});\ \mathbf{u} = \bar{\mathbf{u}} \text{ on } \partial \mathcal{B}_u \right\},$$

$$\mathfrak{d}_{FF} \in \mathcal{U}_{\mathfrak{d}_{FF}} := \left\{ \mathfrak{d}_{FF} \in H^1(\mathcal{B}) | \mathfrak{d}_{FF}(\mathbf{x}) \in [0,1],\ \dot{\mathfrak{d}_{FF}} \geq 0,\ \forall \mathbf{x} \in \mathcal{B} \right\},$$

and:

$$\mathfrak{d}_{IFF} \in \mathcal{U}_{\mathfrak{d}_{IFF}} := \left\{ \mathfrak{d}_{IFF} \in H^1(\mathcal{B}) | \mathfrak{d}_{IFF}(\mathbf{x}) \in [0,1],\ \dot{\mathfrak{d}_{IFF}} \geq 0,\ \forall \mathbf{x} \in \mathcal{B} \right\},$$

are extended by the corresponding test functions:

$$\delta\mathbf{u} \in \mathcal{V}_u = \left\{\delta\mathbf{u} \in H^1(\mathcal{B}) | \nabla\delta\mathbf{u} \in L^2(\mathcal{B});\ \delta\mathbf{u} = \mathbf{0} \text{ on } \partial\mathcal{B}_u\right\},$$

$$\delta\mathfrak{d}_{FF} \in \mathcal{V}_{\mathfrak{d}_{FF}} = \left\{\delta\mathfrak{d} \in H^1(\mathcal{B}) | \delta\mathfrak{d}_{FF} \geq 0,\ \forall\mathbf{x} \in \mathcal{B}\right\},$$

and:

$$\delta\mathfrak{d}_{IFF} \in \mathcal{V}_{\mathfrak{d}_{IFF}} = \left\{\delta\mathfrak{d} \in H^1(\mathcal{B}) | \delta\mathfrak{d}_{IFF} \geq 0,\ \forall\mathbf{x} \in \mathcal{B}\right\},$$

where H^1 denotes the Sobolev space. There accordingly, the weak form of the coupled displacement-crack phase-field problem is constructed as:

$$\delta\Pi(\mathbf{u}, \mathfrak{d}_i, \delta\mathbf{u}, \delta\mathfrak{d}_i) = \delta\Pi_{\text{int}}(\mathbf{u}, \mathfrak{d}_i, \delta\mathbf{u}, \delta\mathfrak{d}_i) + \delta\Pi_{\text{ext}}(\mathbf{u}, \delta\mathbf{u}) = 0, \tag{43}$$

After simple algebraic manipulations, the strong form of the field equations can be obtained:

$$\text{div}\boldsymbol{\sigma} + \mathbf{f}_v = \mathbf{0} \text{ in } \mathcal{B} \text{ and } \boldsymbol{\sigma}\cdot\mathbf{n} = \bar{\mathbf{t}} \text{ on } \partial\mathcal{B}_t, \tag{44}$$

$$2(1-\mathfrak{d}_{FF})P_{FF}\mathcal{H}_{FF}(\mathbf{x},t) = \mathcal{G}_{c,FF}\delta_{\mathfrak{d}_{FF}}\gamma(\mathfrak{d}_{FF}, \nabla\mathfrak{d}_{FF}) \text{ in } \mathcal{B} \text{ and } \nabla\mathfrak{d}_{FF}\cdot\mathbf{n} = 0 \text{ on } \partial\mathcal{B}, \tag{45}$$

$$2(1-\mathfrak{d}_{IFF})P_{IFF}\mathcal{H}_{IFF}(\mathbf{x},t) = \mathcal{G}_{c,IFF}\delta_{\mathfrak{d}_{IFF}}\gamma(\mathfrak{d}_{IFF}, \nabla\mathfrak{d}_{IFF}) \text{ in } \mathcal{B} \text{ and } \nabla\mathfrak{d}_{IFF}\cdot\mathbf{n} = 0 \text{ on } \partial\mathcal{B}. \tag{46}$$

In the previous expressions, div[•] is the divergence operator. The Cauchy stress tensor $\boldsymbol{\sigma}$ can be expressed in terms of the effective stress tensor $\bar{\boldsymbol{\sigma}}$ via: $\boldsymbol{\sigma} = (1-\mathfrak{d}_{FF})^2\bar{\boldsymbol{\sigma}}_{FF} + (1-\mathfrak{d}_{IFF})^2\bar{\boldsymbol{\sigma}}_{IFF}$ with $\bar{\boldsymbol{\sigma}}_{FF} = \mathbb{C}^e_{FF} : \boldsymbol{\varepsilon}$ and $\bar{\boldsymbol{\sigma}}_{IFF} = \mathbb{C}^e_{IFF} : \boldsymbol{\varepsilon}^e$. With respect to the crack driving forces defined in Eqs.(45) and (46), it is worth mentioning that fiber failure only attains elastic deformation, whereas inter-fiber failure is characterized by the evolution of plastic and elastic strains. Here, P_{FF} and P_{IFF} are activation flags for current crack driving forces for fiber and inter-fiber failure, respectively, and are activated if and only if their respective Puck failure criterion has been met. Accordingly, for fiber failure one can define:

$$\mathcal{H}_{FF}(\mathbf{x},t) = \xi^e_{FF}\left[\langle\frac{\max\limits_{\tau\in[0,t]}\hat{\Psi}^e_{FF}(\mathbf{x},\tau)}{\hat{\Psi}^e_{FF,init}} - 1\rangle_+\right], \tag{47}$$

whereas for inter-fiber failure we adopt the crack driving force proposed by the authors in [54]:

$$\mathcal{H}_{IFF}(\mathbf{x},t) = \xi^e_{IFF}\left[\langle\frac{\max\limits_{\tau\in[0,t]}\hat{\Psi}^e_{IFF}(\mathbf{x},\tau)}{\hat{\Psi}^e_{IFF,init}} - 1\rangle_+\right] + \xi^p\left[\langle\frac{\hat{\Psi}^p}{\hat{\Psi}^p_{init}} - 1\rangle_+\right]. \tag{48}$$

It is worth mentioning that both $\mathcal{H}_{FF}$ and $\mathcal{H}_{IFF}$ ensure the positive evolution of the respective phase-field variables, i.e. $\dot{\mathfrak{d}}_{FF} \geq 0$ and $\dot{\mathfrak{d}}_{IFF} \geq 0$. Moreover, $\hat{\Psi}^e_{FF}$ is the maximum reached effective elastic energy for fiber failure and ξ^e_{FF} is a dimensionless parameter that characterizes the activation of fracture due to the elastic contribution but also governs the post-peak behaviour for inter-fiber failure. Similarly, $\hat{\Psi}^e_{IFF}$ is the maximum ever reached effective elastic energy for inter-fiber failure, $\hat{\Psi}^e_{IFF,init}$ is the effective elastic energy for fracture initiation for inter-fiber failure, and ξ^e_{IFF} is a dimensionless parameter associated with the activation of fracture due to the elastic contribution, $\hat{\Psi}^p$ stands for the effective plastic energy, $\hat{\Psi}^p_{init}$ is the effective plastic energy for fracture initiation, and ξ^p is a parameter that tracking the activation of plastic-induced fracture.

Owing to the regularity of the energetic functions, first-order optimality condition is sufficient to ensure stability and energy balance leading to the following Karush-Kuhn-Tucker (KKT) conditions:

$$\dot{\mathfrak{d}_{FF}} \geq 0 \text{ and } \dot{\mathfrak{d}_{IFF}} \geq 0, \tag{49}$$

$$2(1-\mathfrak{d}_{FF})P_{FF}\mathcal{H}_{FF}(\mathbf{x},t) - \mathcal{G}_{c,FF}\delta_{\mathfrak{d}_{FF}}\gamma(\mathfrak{d}_{FF},\nabla\mathfrak{d}_{FF}) \leq 0, \tag{50}$$

$$2(1-\mathfrak{d}_{IFF})P_{IFF}\mathcal{H}_{IFF}(\mathbf{x},t) - \mathcal{G}_{c,IFF}\delta_{\mathfrak{d}_{IFF}}\gamma(\mathfrak{d}_{IFF},\nabla\mathfrak{d}_{IFF}) \leq 0, \tag{51}$$

$$\left[2(1-\mathfrak{d}_{FF})P_{FF}\mathcal{H}_{FF}(\mathbf{x},t) - \mathcal{G}_{c,FF}\delta_{\mathfrak{d}_{FF}}\gamma(\mathfrak{d}_{FF},\nabla\mathfrak{d}_{FF})\right]\dot{\mathfrak{d}_{FF}} = 0, \tag{52}$$

$$\left[2(1-\mathfrak{d}_{IFF})P_{IFF}\mathcal{H}_{IFF}(\mathbf{x},t) - \mathcal{G}_{c,IFF}\delta_{\mathfrak{d}_{IFF}}\gamma(\mathfrak{d}_{IFF},\nabla\mathfrak{d}_{IFF})\right]\dot{\mathfrak{d}_{IFF}} = 0. \tag{53}$$

4. Finite element implementation

In this section, the finite element implementation of the proposed multi phase-field fracture model for long fiber reinforced composites is outlined. The specific operations rely on the framework proposed in [55]. Furthermore, as discussed below, in this investigation, a staggered solution scheme is used for the coupled system of equations. Alternative solution procedures as those given in [56, 57] can be also applicable with relatively minor modifications, which is a task beyond the scope of the present paper.

The solution of the proposed elasto-plastic multi phase-field fracture problem is obtained after discretizing the space using the Finite Element Method (FEM). This means, the continuous domain of the body $\mathcal{B}$ is approximated by a discrete domain $\mathcal{B}^h$ that is formed by a finite number of disjoints elements $\mathcal{B}^e$. There accordingly, the infinite-dimensional function spaces $\mathcal{U}$ and $\mathcal{V}$ are approximated by the corresponding finite-dimensional subspaces $\mathcal{U}^h$ and $\mathcal{V}^h$, imposing the same conditions on the boundaries.

The interpolation of the continuous fields $\mathbf{u}^e$, $\mathfrak{d}^e_{FF}$, and $\mathfrak{d}^e_{IFF}$ is realized via the use of the element-based shape functions:

$$\mathbf{u}^e = \sum_{i=1}^{N_{node}} \mathbf{N}^u_i \mathbf{u}^e_i, \quad \mathfrak{d}^e_{FF} = \sum_{i=1}^{N_{node}} N^{\mathfrak{d}}_i \mathfrak{d}^e_{FF,i}, \quad \mathfrak{d}^e_{IFF} = \sum_{i=1}^{N_{node}} N^{\mathfrak{d}}_i \mathfrak{d}^e_{IFF,i} \tag{54}$$

where $\mathbf{N}^u_i$ and $N^{\mathfrak{d}}_i$ are the shape functions associated with node i for the displacement field $\mathbf{u}^e_i$ and the two phase-field values $\mathfrak{d}^e_{FF,i}$, $\mathfrak{d}^e_{IFF,i}$, respectively, for N_{Node} in the finite element. The derivatives associated with the fields $\mathbf{u}$, $\mathfrak{d}_{FF}$, and $\mathfrak{d}_{IFF}$ are expressed as follows, respectively:

$$\boldsymbol{\varepsilon}^e = \sum_{i=1}^{N_{node}} \mathbf{B}^u_i \mathbf{u}^e_i, \quad \nabla\mathfrak{d}^e_{FF} = \sum_{i=1}^{N_{node}} \mathbf{B}^{\mathfrak{d}}_i \mathfrak{d}^e_{FF,i}, \quad \nabla\mathfrak{d}^e_{IFF} = \sum_{i=1}^{N_{node}} \mathbf{B}^{\mathfrak{d}}_i \mathfrak{d}^e_{IFF,i},$$

where $\mathbf{B}^u_i$ and $\mathbf{B}^{\mathfrak{d}}_i$ are the corresponding spatial derivatives of the shape functions.

Similarly, the test functions and their respective derivatives take the form:

$$\delta\mathbf{u}^e = \sum_{i=1}^{N_{node}} \mathbf{N}^u_i \delta\mathbf{u}^e_i, \quad \delta\mathfrak{d}^e_{FF} = \sum_{i=1}^{N_{node}} \mathbf{N}^{\mathfrak{d}}_i \delta\mathfrak{d}^e_{FF,i}, \quad \delta\mathfrak{d}^e_{IFF} = \sum_{i=1}^{N_{node}} \mathbf{N}^{\mathfrak{d}}_i \delta\mathfrak{d}^e_{IFF,i} \tag{55}$$

$$\delta\boldsymbol{\varepsilon}^e = \sum_{i=1}^{N_{node}} \mathbf{B}^u_i \delta\mathbf{u}^e_i, \quad \nabla\delta\mathfrak{d}^e_{FF} = \sum_{i=1}^{N_{node}} \mathbf{B}^{\mathfrak{d}}_i \delta\mathfrak{d}^e_{FF,i}, \quad \nabla\delta\mathfrak{d}^e_{IFF} = \sum_{i=1}^{N_{node}} \mathbf{B}^{\mathfrak{d}}_i \delta\mathfrak{d}^e_{IFF,i}.$$

The element residual vectors for the displacement and the two phase-fields can be reduced to:

$$\mathbf{r}^{\mathbf{u}}_e = \int_{\mathcal{B}^e} \left[(1-\mathfrak{d}_{FF})^2(\mathbf{B}^u)^T\bar{\boldsymbol{\sigma}}_{FF} + (1-\mathfrak{d}_{IFF})^2(\mathbf{B}^u)^T\bar{\boldsymbol{\sigma}}_{IFF}\right] \mathrm{d}\mathcal{B} - \int_{\mathcal{B}^e} (\mathbf{N}^u)^T\mathbf{f}_v \mathrm{d}\mathcal{B} - \int_{\partial\mathcal{B}^e_u} (\mathbf{N}^u)^T\overline{\mathbf{u}}\mathrm{d}\partial\mathcal{B}, \tag{56}$$

$$\mathbf{r}_e^{\mathfrak{d}_{FF}} = \int_{\mathcal{B}^e} \left\{ \left[\frac{\mathcal{G}_{c,FF}}{l_{FF}} \mathfrak{d}_{FF} - 2(1-\mathfrak{d}_{FF}) P_{FF} \mathcal{H}_{FF}(\mathbf{x},t) \right] (N^{\mathfrak{d}})^T + \mathcal{G}_{c,FF} l_{FF} (\mathbf{B}^{\mathfrak{d}})^T \nabla \mathfrak{d}_{FF} \right\} \mathrm{d}\mathcal{B}, \tag{57}$$

$$\mathbf{r}_e^{\mathfrak{d}_{IFF}} = \int_{\mathcal{B}^e} \left\{ \left[\frac{\mathcal{G}_{c,IFF}}{l_{IFF}} \mathfrak{d}_{IFF} - 2(1-\mathfrak{d}_{IFF}) P_{IFF} \mathcal{H}_{IFF}(\mathbf{x},t) \right] (N^{\mathfrak{d}})^T + \mathcal{G}_{c,IFF} l_{IFF} (\mathbf{B}^{\mathfrak{d}})^T \nabla \mathfrak{d}_{IFF} \right\} \mathrm{d}\mathcal{B}. \tag{58}$$

Notice that the system of equations is non-linear due to the presence of plasticity and fracture. Hence, after assembling, one must resort to incremental iterative solvers such as Newton-Raphson (NR). It is clear that the phase-field equations, see Eqs.(57)-(58), are uncoupled from each other, but coupled with the equilibrium equation, see Eq.(56). However, the global system of equations is solved using an alternating minimization scheme to decouple the displacement and the phase-field problem (fixed point minimization algorithm).

The corresponding Newton-Raphson iteration for the global assembled system at step $(n+1)$ can be written as:

$$\begin{bmatrix} \mathbf{u} \\ \mathfrak{d}_{FF} \\ \mathfrak{d}_{IFF} \end{bmatrix}_{n+1} = \begin{bmatrix} \mathbf{u} \\ \mathfrak{d}_{FF} \\ \mathfrak{d}_{IFF} \end{bmatrix}_{n} - \begin{bmatrix} K^{\mathbf{uu}} & 0 & 0 \\ 0 & K^{\mathfrak{d}_{FF}\mathfrak{d}_{FF}} & 0 \\ 0 & 0 & K^{\mathfrak{d}_{IFF}\mathfrak{d}_{IFF}} \end{bmatrix}^{-1}_{n+1} \begin{bmatrix} \mathbf{r}^{\mathbf{u}} \\ \mathbf{r}^{\mathfrak{d}_{\mathbf{FF}}} \\ \mathbf{r}^{\mathfrak{d}_{\mathbf{IFF}}} \end{bmatrix}_{n}, \tag{59}$$

where the corresponding element stiffness matrices read:

$$K_e^{\mathbf{uu}} = \frac{\partial \mathbf{r}_e^{\mathbf{u}}}{\partial \mathbf{u}^e} = \int_{\mathcal{B}} \left[(\mathbf{B}^u)^T \mathbb{C}^{ep\mathfrak{d}} \mathbf{B}^u \right] \mathrm{d}\mathcal{B},$$

$$K_e^{\mathfrak{d}_{FF}\mathfrak{d}_{FF}} = \frac{\partial \mathbf{r}_e^{\mathfrak{d}_{FF}}}{\partial \mathfrak{d}_{FF}^e} = \int_{\mathcal{B}} \left\{ \left[\frac{\mathcal{G}_{c,FF}}{l_{FF}} + 2P_{FF}\mathcal{H}_{IFF}(\mathbf{x},t) \right] \mathbf{N}^{\mathfrak{d}} (\mathbf{N}^{\mathfrak{d}})^T + \mathcal{G}_{c,FF} l_{FF} (\mathbf{B}^{\mathfrak{d}})^T \mathbf{B}^{\mathfrak{d}} \right\} \mathrm{d}\mathcal{B},$$

$$K_e^{\mathfrak{d}_{IFF}\mathfrak{d}_{IFF}} = \frac{\partial \mathbf{r}_e^{\mathfrak{d}_{IFF}}}{\partial \mathfrak{d}_{IFF}^e} = \int_{\mathcal{B}} \left\{ \left[\frac{\mathcal{G}_{c,IFF}}{l_{IFF}} + 2P_{IFF}\mathcal{H}_{IFF}(\mathbf{x},t) \right] \mathbf{N}^{\mathfrak{d}} (\mathbf{N}^{\mathfrak{d}})^T + \mathcal{G}_{c,IFF} l_{IFF} (\mathbf{B}^{\mathfrak{d}})^T \mathbf{B}^{\mathfrak{d}} \right\} \mathrm{d}\mathcal{B},$$

and $\mathbb{C}^{ep\mathfrak{d}}$ is the material consistent tangent.

The above system of equations has been implemented in the general-purpose FE package `ABAQUS` to take advantage of the in-built non-linear solvers and automatic time-stepping methods. Hence, a user-defined `UMAT` is written for the solution of equilibrium equations associated with the displacement field whereas `UEL` is utilized for solving the phase-field fracture problem. A three-layer structure (for each ply) is adopted as shown in Figure 2, corresponding to the displacement field and the two phase-fields, where each of the layers shares the same nodes but has different stiffness and Degrees of Freedom (DOFs). The elements in the first layer contain three DOFs (two for the 2D case), whereas the second and third layers have one DOF of phase-field $\mathfrak{d}_{FF}$ and $\mathfrak{d}_{IFF}$, respectively. The `UMAT` is called at each Gauss point in the first layer to evaluate the constitutive behavior of the displacement field. To be specific, the anisotropic elasto-plastic model presented in Section 2 provides the elastic and plastic strains along with their corresponding effective stresses. Subsequently, at each Gauss point, the stresses are checked against the Puck failure criteria to predict the failure modes and activation flags. Since the degradation of the energy entirely depends on the type of failure (i.e fiber failure or inter-fiber failure) different driving forces are computed accordingly. The `UEL` is called at each element in the second and third layers. Depending on the computed driving force and activation flags, the corresponding phase-field values are computed.

The corresponding layers in the system disseminate through the common block. After each increment, the solution dependent variables are stored as `STATEV` in `UMAT` to post-process the results.

5. Representative applications

In this section, different numerical examples are presented showing the predictive capabilities of the proposed formulation.

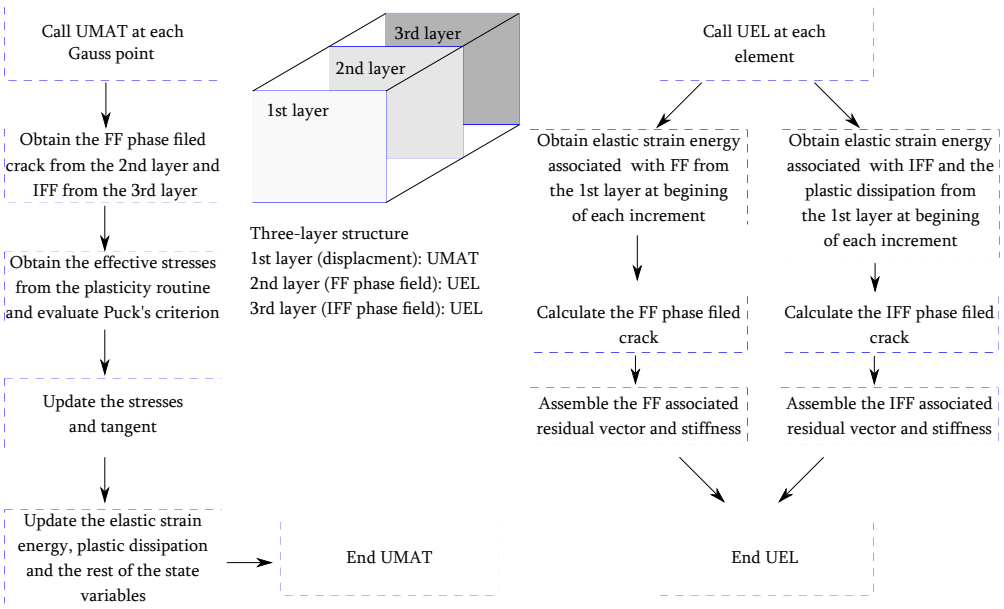

Figure 2: Three-layer structure of `ABAQUS` subroutine.

5.1. Material parameters

Herein, two different materials are considered, CFRP (IM7/8552) and GFRP (E-Glass/MY750), and the proposed model is calibrated on the experimental data provided in [58, 13, 59] and the references therein given. The elastic material constants of the CFRP and GFRP materials are listed in Table 2.

Material	E_{11} (GPa)	E_{22} (GPa)	G_{12} (GPa)	ν_{12}	ν_{23}
CFRP	171.42	9.08	5.39	0.0169	0.38
GFRP	45.6	16.2	5.83	0.099	0.4

Table 2: CFRP and GFRP: elastic properties.

Following the procedure presented in [60], the yield function parameters ζ_i $(i = 1, 4)$ that characterize the onset of yielding are listed in Table 3 for CFRP and GFRP.

Material	ζ_1	ζ_2	ζ_3	ζ_4
CFRP	0.00262532	0.00179157	-0.0097352	0.00411623
GFRP	0.00338351	0.00230897	-0.0110519	0.00530498

Table 3: CFRP and GFRP: yielding parameters ζ_i at the onset of yielding.

The plastic potential function parameters ς_i $(i = 2, 3)$ are obtained for the CFRP and GFRP for the plastic Poisson's ratios given in Table 4.

Material	μ^p_{12}	ν^p_{23}
CFRP	1.0	0.38
GFRP	1.0	0.4

Table 4: CFRP and GFRP: plastic Poisson's ratios.

Furthermore, for the Puck failure criteria, the strength properties are listed in Table 5 for the CFRP and GFRP materials.

Material	$R_{\parallel}^{t}$ (MPa)	$R_{\parallel}^{c}$ (MPa)	$R_{\perp}^{t}$ (MPa)	$R_{\perp}^{c}$ (MPa)	$R_{\parallel\perp}$ (MPa)
CFRP	2323.5	1200.1	62.3	199.8	92.3
GFRP	1280	800	40	145	73.3

Table 5: CFRP and GFRP: strength properties.

In addition, the fracture properties and phase-field parameters are reported in Table 6 for CFRP and GFRP.

Material	$\mathcal{G}_{c,FF}$ (N/mm)	$\mathcal{G}_{c,IFF}$ (N/mm)	l_{FF} (mm)	l_{IFF} (mm)	$\xi_{e,FF}$ (-)	$\xi_{e,IFF}$ (-)	ξ_{p} (-)
CFRP	81.5	0.2774	0.273	0.07	50 (assumed)	0.5 (assumed)	0.5 (assumed)
GFRP	64	1.8	0.19	1.9	50 (assumed)	0.5 (assumed)	0.5 (assumed)

Table 6: CFRP and GFRP: fracture properties and phase-field parameters.

5.2. Validation of implementation

Herein, the validity and potential of the proposed formulation are assessed utilizing a single element FE model. The CFRP 3D brick element's side length is set to be 1 mm. Four load cases (corresponding to four different failure modes) are considered for which the fiber direction is taken as reference: (i) longitudinal uniaxial tension, (ii) transverse uniaxial tension, (iii) transverse uniaxial compression, and (iv) in-plane shear.

With respect to the loading, in all the four cases, the element is loaded under displacement control with constant increment $\Delta u = 0.0001$ mm in order to ensure the stability of the numerical solution.

The numerical results of the first load case (longitudinal uniaxial tension) are depicted in Figure 3. In this plot, it can be observed that, throughout the first part of the evolution, i.e. before the material strength is reached, linear elastic behavior is retrieved. Once the fiber failure onset criterion is satisfied, the fiber failure phase-field crack variable commences evolving.

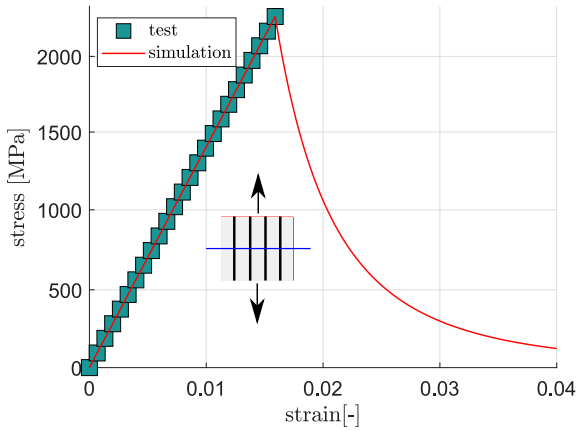

Figure 3: Numerical simulations and experimental results: FF Mode.

The results from the second loading case (transverse uniaxial tension) are shown in Figure 4.a. Herein, the pre-failure non-linearities are observed due to the assumption of elasto-plastic behavior in a matrix-dominated response. Once the material strength is reached and the Puck inter-fiber failure criterion is met,

the inter-fiber phase-field crack begins to evolve. The orientation of the fracture plane is stored as a state-dependent variable. Hence, under uniaxial tensile conditions, the angle of the fracture plane is obtained to be around $\theta_{fp} = 0°$, which is inline with Mode A in Puck's theory. Similarly, for the third load case (transverse uniaxial compression), the Puck inter-fiber failure criterion is violated, see Figure 4.b. However, in this case, the angle of the fracture plane is predicted to be around $\theta_{fp} = 53°$ i.e. Mode C according to the Puck theory.

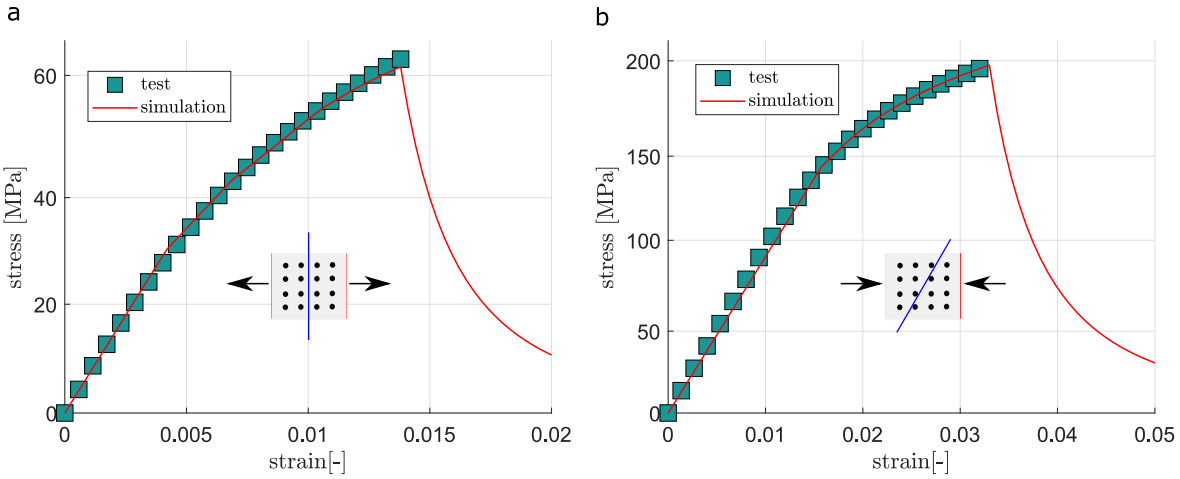

Figure 4: Numerical simulations and experimental results: (a) IFF Mode A and (b) IFF Mode C.

In the fourth loading case, the applicability of the proposed model for triggering the failure of the CFRP material under in-plane shear is examined. Similarly, the elasto-plastic model is used to predict the experimentally observed prominent pre-failure non-linearities due to plasticity associated with such load cases, see Figure 5.a. In accordance with Puck theory, inter-fiber failure with a fracture plane angle of $\theta_{fp} = 0°$ is predicted. The simultaneous evolution of the plastic deformations and the cracking process is depicted in Figure 5.b.

The ability of the proposed multi phase-field model to predict the different fracture mechanisms observed in long fiber reinforced composites can clearly be noticed. Furthermore, in all the examined loading cases, a very satisfactory agreement between the experimental data (up to failure [13]) and the numerical predictions can be noticed.

5.3. Demonstrative examples

In the preset section, the potential of the proposed formulation to capture the anisotropic fracture behavior of long fiber composites is demonstrated. For this purpose, a FE model that mimics a plate with an initial notch made of GFRP composites is constructed. The plate is partitioned into four regions to allow assigning different fiber orientations to each one. The geometry, partitioning, boundary conditions, and loading are depicted in Figure 6. Three different fiber orientation arrangements are considered in the present study, which are listed in Table 7.

	FO of Region 1	FO of Region 2	FO of Region 3	FO of Region 4
Case 1	0°	0°	0°	0°
Case 2	−45°	−45°	0°	0°
Case 3	0°	0°	−45°	−45°

Table 7: GFRP plate with an initial notch: fiber orientation (FO) arrangements for the three different cases.

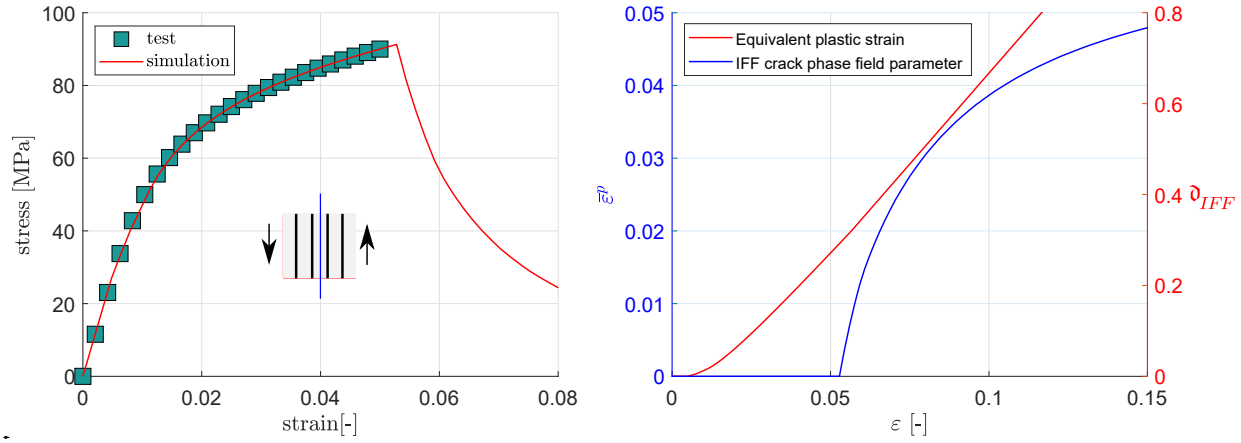

Figure 5: Numerical simulations and experimental results of the pure shear case: (a) stress-strain response and (b) simultaneous evolution of the plastic deformations and the inter-fiber cracking process.

The domain is discretized employing 251000 4-node quadrilateral plane stress elements. In all the three cases, the plate is loaded under displacement control with constant increment $\Delta u = 0.0001$ mm.

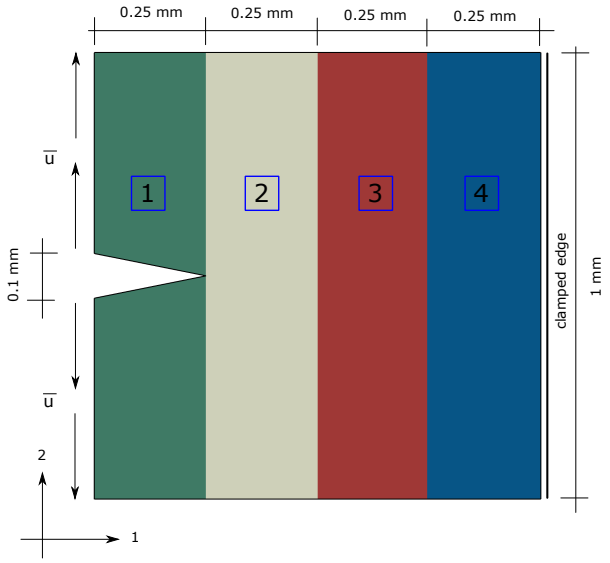

Figure 6: GFRP plate with an initial notch: specimen geometry and boundary conditions.

The numerical predictions obtained from the three different cases are presented in Figures 7-9. Inline with previous research [40], matrix-dominated cracking evolution is predicted. Figures 7-9 depicts the different phases of the cracking evolution whereby significant crack kinks between adjacent layers are obtained stemming from the differences between the corresponding material orientations. Hence, the capability of the proposed implemented model to predict the anisotropic fracture behavior of long fiber reinforced composites can be observed.

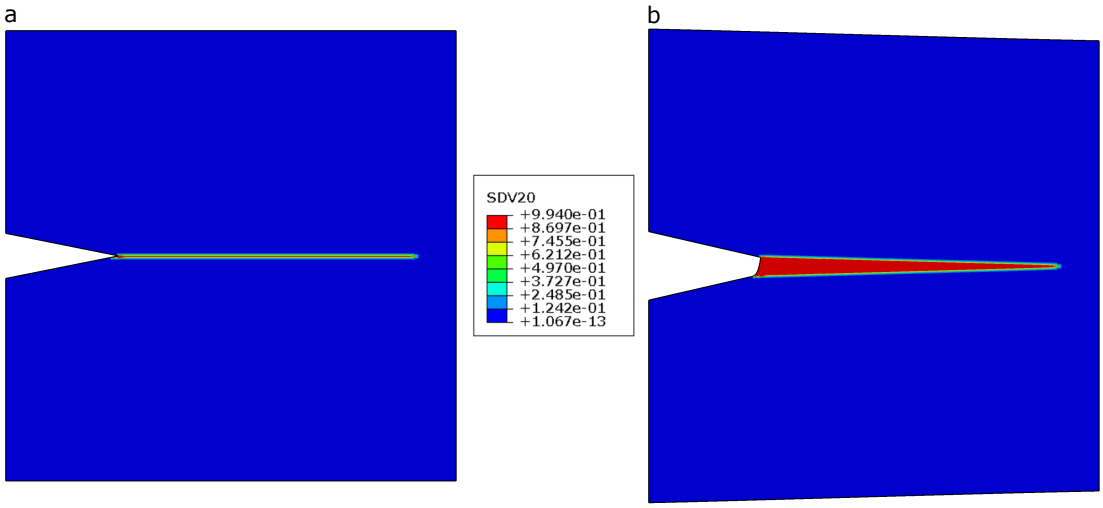

Figure 7: Inter-fiber phase-field crack (SDV20) from case 1 of the GFRP plate in: (a) undeformed configuration and (b) deformed configuration.

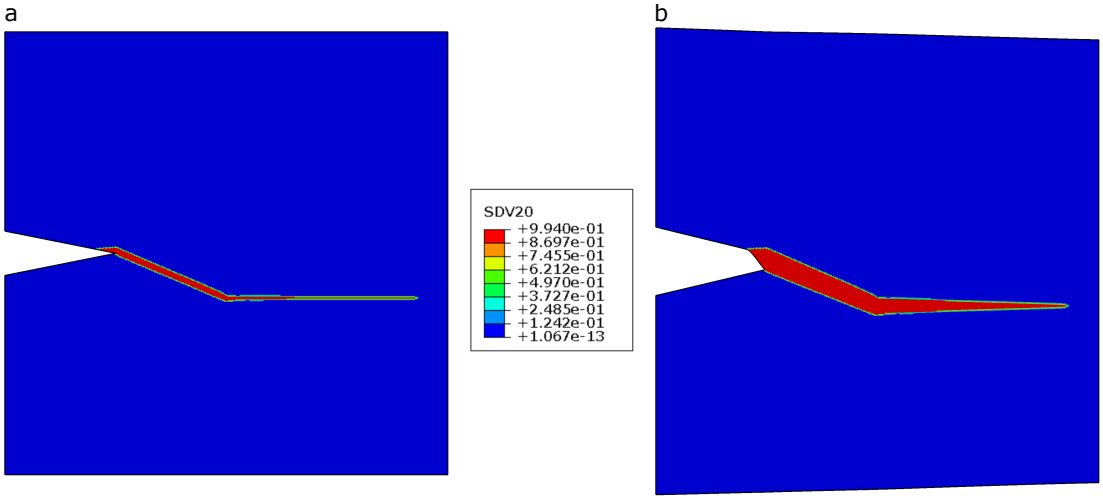

Figure 8: Inter-fiber phase-field crack (SDV20) from case 2 of the GFRP plate in: (a) undeformed configuration and (b) deformed configuration.

5.4. Open-hole tension problem

The proposed multi phase-field formulation is applied to predict the progressive failure of an open-hole fiber reinforced specimen. The geometric definition of the specimen under consideration is shown in Figure 10, replicating the 3 mm thick CFRP quasi-isotropic $[90°/0°/\pm 45°]_{3s}$ laminate investigated in [13] employing a CDM model. The specimen is discretized employing 475008 8-node 3D brick elements. Two elements per ply are used. Inline with [13], the following in-situ strengths are incorporated into the model based on the formulation proposed in [61], see Table 8. The specimen is loaded under tension until failure via displacement control with constant increment $\Delta u = 0.0001$ mm.

The numerical-experimental correlation corresponding to the load-displacement curve is depicted in Figure 11. In both cases (numerical and experimental) and before the maximum strength is reached, a

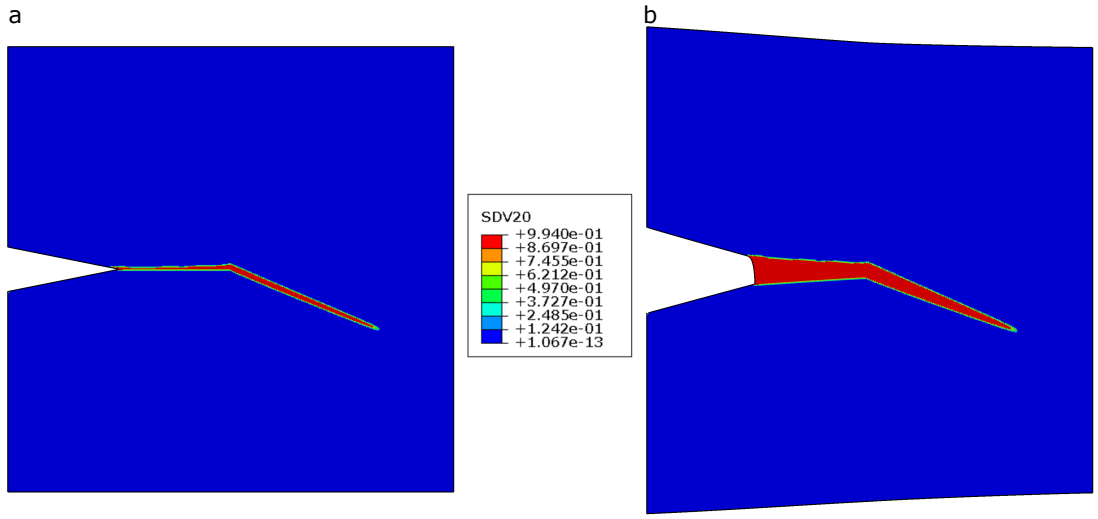

Figure 9: Inter-fiber phase-field crack (SDV20) from case 3 of the GFRP plate in: (a) undeformed configuration and (b) deformed configuration.

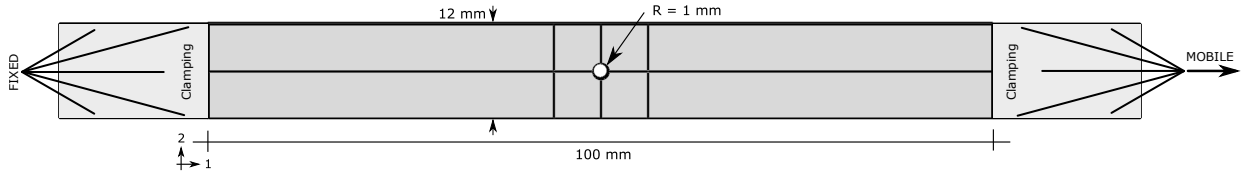

Figure 10: open-hole tension problem: specimen geometry and boundary conditions.

	$R^t_\perp$ (MPa)	$R_{\parallel\perp}$ (MPa)
Embedded plies	106.2	101.4
Outer plies	130.2	107.0

Table 8: CFRP: in-situ strengths properties.

bilinear evolution of the curve is observed. Therein, an initial linear evolution stage followed by a quasi-linear evolution due to the initiation and development of damage and failure. Despite the fact that the numerically predicted initial linear stage of the curve matches perfectly the experimental results, in the quasi-linear stage, a stiffer response is predicted. Such discrepancies are attributed to the fact that inter-laminar failures are not considered appropriately in this simulation and hence the interaction between intra-laminar and inter-laminar fracture events. However, a satisfactory agreement between the numerical and the experimental data can be observed.

The inter-fiber and fiber failure patterns at different loading stages (40%, 65%, 85% of the ultimate load, and rupture) are shown in Figures 12 and 13, respectively. As depicted in Figure 12, an X-shaped inter-fiber crack pattern is observed in the 90° ply. With respect to the 0° ply, tensile fiber failure is predicted, see Figure 13. Inline with [13], a net section failure mode is predicted in which the cracks are initially concentrated around the hole and subsequently propagate perpendicular to the loading direction.

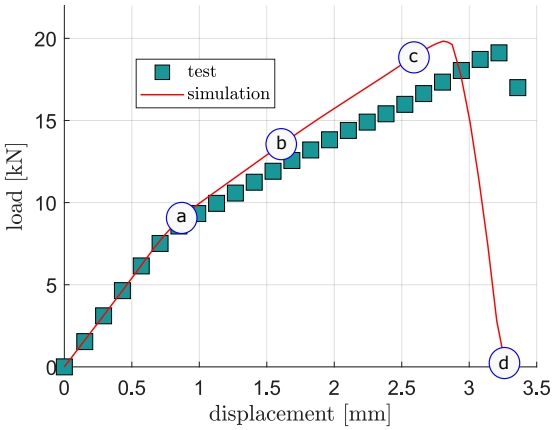

Figure 11: Open-hole tension problem: Numerical-experimental correlation corresponding to the load-displacement curve.

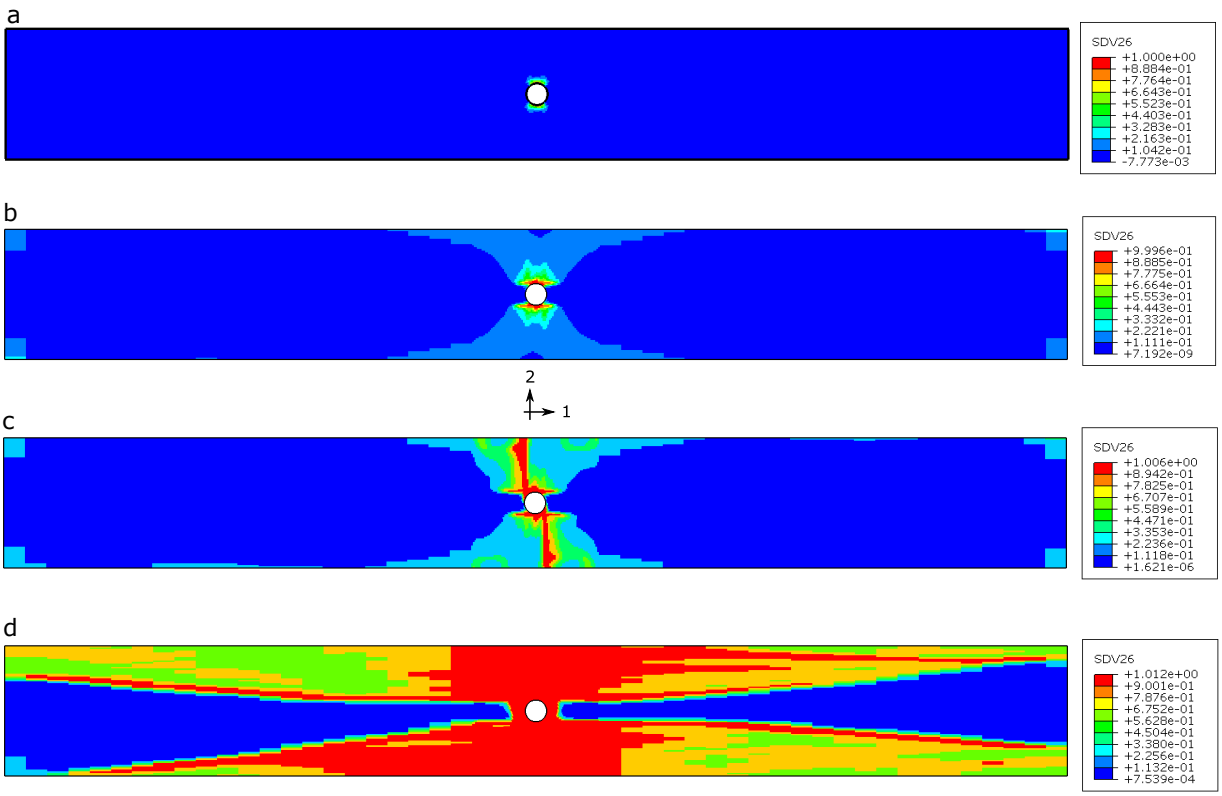

Figure 12: Open-hole tension problem: IFF phase-field crack (SDV26) evolution in the outer90° layer at different loading stages: (a) 60% of the ultimate load, (b) 80% of the ultimate load, (c) 100% of the ultimate load, and (d) rupture.

6. Conclusions

Relying on the Puck's failure theory, fracture events in long fiber reinforced composites at ply level can be mainly classified into fiber and inter-fiber (matrix-dominated) cracking. In order to account for

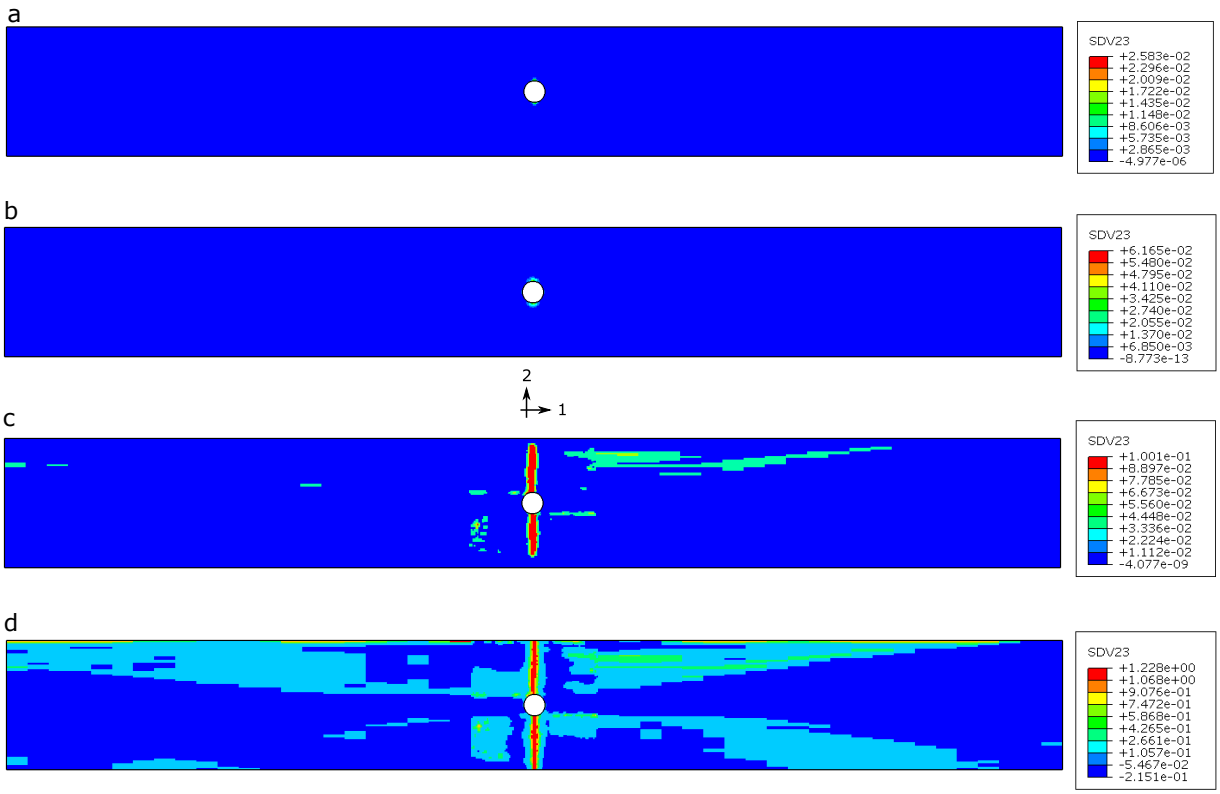

Figure 13: Open-hole tension problem: FF phase-field crack (SDV23) evolution in the outer0° layer at different loading stages: (a) 60% of the ultimate load, (b) 80% of the ultimate load, (c) 100% of the ultimate load, and (d) rupture.

such failure mechanisms into the Phase-Field (PF) approach of fracture, a novel multi phase-field model has been proposed. Particularly, in the present investigation, we have formulated a novel model that is characterized by: (i) the consideration of a single damage-like phase-field variable for each failure mechanism with corresponding fracture energy and length scale, and (ii) the integration of an invariant-based plasticity model for characterizing matrix-failure dominated states.

The proposed formulation has been carefully derived via a multi-field variational formalism with the specific incorporation of the multiple dissipative mechanisms within the spirit of the PF method. Special attention has been also devoted to the consistent numerical implementation.

On the applicability side, several illustrative examples have evidenced the reliability of the proposed formulation. Finally, it is worth noting that this work can be conceived as a first attempt whereby phenomenological failure criteria for long fiber reinforced composites are integrated into PF methods. Further developments may concern the corresponding extension to fatigue [62, 63] and the combination with interface-like cracking models for triggering complex fracture patterns in composites. Dynamic fracture is of high-interest in a wide variety of engineering applications. In this view, the proposed PF model will be extended incorporating the rate-dependent material models presented in [64, 65].

Acknowledgments

JR is grateful to the Consejería de Economía y Conocimiento of the Junta de Andalucía (Spain) for financial support under the contract US-1265577-Programa Operativo FEDER Andalucía 2014-2020.

References

[1] M. Ortiz, A. Pandolfi, Finite deformation irreversible cohesive elements for three-dimensional crack-propagation analysis, International Journal for Numerical Methods in Engineering 44 (1999) 1267–1282. doi:10.1002/(SICI)1097-0207(19990330)44:9¡1267::AID-NME486¿3.0.CO;2-7.

[2] A. Ortega, P. Maimí, E. González, D. Trias, Characterization of the translaminar fracture cohesive law, Composites Part A: Applied Science and Manufacturing 91, Part 2 (2016) 501 – 509, compTest 2015. doi:10.1016/j.compositesa.2016.01.019.

[3] A. Turon, P. Camanho, J. Costa, C. Dávila, A damage model for the simulation of delamination in advanced composites under variable-mode loading, Mechanics of Materials 38 (11) (2006) 1072 – 1089. doi:10.1016/j.mechmat.2005.10.003.

[4] J. Reinoso, M. Paggi, A. Blázquez, A nonlinear finite thickness cohesive interface element for modeling delamination in fibre-reinforced composite laminates, Composites Part B: Engineering (2017) 116 – 128doi:10.1016/j.compositesb.2016.10.042.

[5] P. P. Camanho, C. G. Davila, M. F. de Moura, Numerical simulation of mixed-mode progressive delamination in composite materials, Journal of Composite Materials 37 (16) (2003) 1415–1438. doi:10.1177/0021998303034505.

[6] L. Távara, J. Reinoso, A. Blázquez, V. Mantič, On the 3d extension of failure models for adhesive joints under mixed-mode fracture conditions: Lebim and czm, Theoretical and Applied Fracture Mechanics 100 (2019) 362 – 376.

[7] P. Ladevèze, E. L. Dantec, Damage modelling of the elementary ply for laminated composites, Composites Science and Technology 43 (3) (1992) 257 – 267. doi:10.1016/0266-3538(92)90097-M.

[8] A. Quintanas-Corominas, P. Maimí, E. Casoni, A. Turon, J. Mayugo, G. Guillamet, M. Vázquez, A 3D transversally isotropic constitutive model for advanced composites implemented in a high performance computing code, European Journal of Mechanics - A/Solids 71 (2018) 278 – 291. doi:10.1016/j.euromechsol.2018.03.021.

[9] P. Maimí, P. Camanho, J. Mayugo, A. Turon, Matrix cracking and delamination in laminated composites. Part I: Ply constitutive law, first ply failure and onset of delamination, Mechanics of Materials 43 (4) (2011) 169 – 185. doi:10.1016/j.mechmat.2010.12.003.

[10] P. Maimí, P. Camanho, J. Mayugo, C. Dávila, A continuum damage model for composite laminates: Part II – Computational implementation and validation, Mechanics of Materials 39 (10) (2007) 909 – 919. doi:10.1016/j.mechmat.2007.03.006.

[11] P. Camanho, P. Maimí, C. Dávila, Prediction of size effects in notched laminates using continuum damage mechanics, Composites Science and Technology 67 (13) (2007) 2715 – 2727. doi:10.1016/j.compscitech.2007.02.005.

[12] F. Van der Meer, L. Sluys, Continuum models for the analysis of progressive failure in composite laminates, Journal of Composite Materials 43 (20) (2009) 2131 – 2156. doi:10.1177/0021998309343054.

[13] J. Reinoso, G. Catalanotti, A. Blázquez, P. Areias, P. Camanho, F. París, A consistent anisotropic damage model for laminated fiber-reinforced composites using the 3d-version of the puck failure criterion, International Journal of Solids and Structures (2017) 37 – 53doi:10.1016/j.ijsolstr.2017.07.023.

[14] G. Francfort, J.-J. Marigo, Revisiting brittle fracture as an energy minimization problem, Journal of the Mechanics and Physics of Solids 46 (8) (1998) 1319 – 1342. doi:10.1016/S0022-5096(98)00034-9.

[15] B. Bourdin, G. Francfort, J. Marigo, Numerical experiments in revisited brittle fracture, Journal of the Mechanics and Physics of Solids 48 (4) (2000) 797 – 826. doi:10.1016/S0022-5096(99)00028-9.

[16] B. Bourdin, G. Francfort, J. Marigo, The variational approach to fracture, Journal of Elasticity 91 (1) (2008) 5 – 148. doi:10.1007/s10659-007-9107-3.

[17] C. Miehe, F. Welschinger, M. Hofacker, Thermodynamically consistent phase-field models of fracture: Variational principles and multi-field FE implementations, International Journal for Numerical Methods in Engineering 83 (10) (2010) 1273 – 1311. doi:10.1002/nme.2861.

[18] C. Miehe, M. Hofacker, L.-M. Schänzel, F. Aldakheel, Phase field modeling of fracture in multi-physics problems. Part II. coupled brittle-to-ductile failure criteria and crack propagation in thermo-elastic–plastic solids, Computer Methods in Applied Mechanics and Engineering 294 (2015) 486 – 522. doi:10.1016/j.cma.2014.11.017.

[19] C. Miehe, L. Schänzel, H. Ulmer, Phase field modeling of fracture in multi-physics problems. Part I. balance of crack surface and failure criteria for brittle crack propagation in thermo-elastic solids, Computer Methods in Applied Mechanics and Engineering 294 (2015) 449 – 485. doi:https://doi.org/10.1016/j.cma.2014.11.016.

[20] P. Farrell, C. Maurini, Linear and nonlinear solvers for variational phase-field models of brittle fracture, International Journal for Numerical Methods in Engineering 109 (5) (201) 648–667. doi:10.1002/nme.5300.

[21] A. Mesgarnejad, B. Bourdin, M. Khonsari, Validation simulations for the variational approach to fracture, Computer Methods in Applied Mechanics and Engineering 290 (2015) 420 – 437. doi:10.1016/j.cma.2014.10.052.

[22] E. Tanné, T. Li, B. Bourdin, J. Marigo, C. Maurini, Crack nucleation in variational phase-field models of brittle fracture, Journal of the Mechanics and Physics of Solids 110 (2018) 80 – 99. doi:10.1016/j.jmps.2017.09.006.

[23] M. Ambati, L. D. Lorenzis, Phase-field modeling of brittle and ductile fracture in shells with isogeometric nurbs-based solid-shell elements, Computer Methods in Applied Mechanics and Engineering 312 (2016) 351–373. doi:10.1016/j.cma.2016.02.017.

[24] R. Alessi, J. Marigo, C. Maurini, S. Vidoli, Coupling damage and plasticity for a phase-field regularisation of brittle, cohesive and ductile fracture: One-dimensional examples, International Journal of Mechanical Sciences 149 (2018) 559 – 576. doi:10.1016/j.ijmecsci.2017.05.047.

[25] E. Martínez-Pañeda, A. Golahmar, C. Niordson, A phase field formulation for hydrogen assisted cracking, Computer Methods in Applied Mechanics and Engineering 342 (2018) 742 – 761. doi:10.1016/j.cma.2018.07.021.

[26] V. Carollo, J. Reinoso, M. Paggi, A 3D finite strain model for intralayer and interlayer crack simulation coupling the phase field approach and cohesive zone model, Composite Structures 182 (2017) 636 – 651. doi:10.1016/j.compstruct.2017.08.095.

[27] V. Carollo, J. Reinoso, M. Paggi, Modeling complex crack paths in ceramic laminates: a novel variational framework

combining the phase field method of fracture and the cohesive zone model, Journal of the European Ceramic Society 38 (8) (2018) 2994–3003. doi:10.1016/j.jeurceramsoc.2018.01.035.
[28] S. Teichtmeister, D. Kienle, F. Aldakheel, M. Keip, Phase field modeling of fracture in anisotropic brittle solids, International Journal of Non-Linear Mechanics 97 (2017) 1 – 21. doi:10.1016/j.ijnonlinmec.2017.06.018.
[29] B. Li, C. Maurini, Crack kinking in a variational phase-field model of brittle fracture with strongly anisotropic surface energy, Journal of the Mechanics and Physics of Solids 125 (2019) 502 – 522. doi:https://doi.org/10.1016/j.jmps.2019.01.010.
URL http://www.sciencedirect.com/science/article/pii/S0022509618308664
[30] J. Clayton, J. Knap, Phase field modeling and simulation of coupled fracture and twinning in single crystals and polycrystals, Computer Methods in Applied Mechanics and Engineering 312 (2016) 447 – 467, phase Field Approaches to Fracture. doi:https://doi.org/10.1016/j.cma.2016.01.023.
URL http://www.sciencedirect.com/science/article/pii/S0045782516300226
[31] A. Shahba, S. Ghosh, Coupled phase field finite element model for crack propagation in elastic polycrystalline microstructures, International Journal of Fracture 219 (1) (2019) 31–64.
[32] A. Dean, S. Sahraee, J. Reinoso, R. Rolfes, Finite deformation model for short fibre reinforced composites: Application to hybrid metal-composite clinching joints, Composite Structures 150 (2016) 162–171.
[33] A. Dean, J. Reinoso, S. Sahraee, R. Rolfes, An invariant-based anisotropic material model for short fiber-reinforced thermoplastics: Coupled thermo-plastic formulation, Composites Part A: Applied Science and Manufacturing 90 (2016) 186–199.
[34] A. Dean, S. Sahraee, J. Reinoso, R. Rolfes, A new invariant-based thermo-plastic model for finite deformation analysis of short fibre reinforced composites: Development and numerical aspects, Composites Part B: Engineering 125 (2017) 241–258.
[35] A. Dean, Material modeling of short fiber reinforced polymeric composites: Theory, numerical aspects, and application, Doctoral degree, dissertation thesis, Leibniz Universität Hannover (2017).
[36] A. Dean, N. Grbic, R. Rolfes, B.-A. Behrens, Macro-mechanical modeling and experimental validation of anisotropic, pressure- and temperature-dependent behavior of short fiber composites, Composite Structures 211 (2019) 630–643. doi:10.1016/j.compstruct.2018.12.045.
[37] O. Gültekin, H. Dal, G. A. Holzapfel, Numerical aspects of anisotropic failure in soft biological tissues favor energy-based criteria: A rate-dependent anisotropic crack phase-field model, Computer Methods in Applied Mechanics and Engineering 331 (2018) 23 – 52. doi:10.1016/j.cma.2017.11.008.
[38] O. Gültekin, H. Dal, G. Holzapfel, A phase-field approach to model fracture of arterial walls: Theory and finite element analysis, Computer Methods in Applied Mechanics and Engineering 312 (2016) 542 – 566. doi:10.1016/j.cma.2016.04.007.
[39] J. Reinoso, A. Arteiro, M. Paggi, P. Camanho, Strength prediction of notched thin ply laminates using finite fracture mechanics and the phase field approach, Composites Science and Technology 150 (2017) 205 – 216. doi:10.1016/j.compscitech.2017.07.020.
[40] A. Quintanas-Corominas, J. Reinoso, E. Casoni, A. Turon, J. Mayugo, A phase field approach to simulate intralaminar and translaminar fracture in long fiber composite materials, Composite Structures (2019). doi:10.1016/j.compstruct.2019.02.007.
[41] R. Alessi, F. Freddi, Phase-field modelling of failure in hybrid laminates, Composite Structures 181 (2017) 9 – 25. doi:10.1016/j.compstruct.2017.08.073.
[42] J. Bleyer, R. Alessi, Phase-field modeling of anisotropic brittle fracture including several damage mechanisms, Computer Methods in Applied Mechanics and Engineering 336 (2018) 213 – 236. doi:https://doi.org/10.1016/j.cma.2018.03.012.
[43] M. Paggi, M. Corrado, J. Reinoso, Fracture of solar-grade anisotropic polycrystalline silicon: A combined phase field–cohesive zone model approach, Computer Methods in Applied Mechanics and Engineering 330 (2018) 123 – 148. doi:https://doi.org/10.1016/j.cma.2017.10.021.
[44] T. Guillén-Hernández, I. García, J. Reinoso, M. Paggi, A micromechanical analysis of inter-fiber failure in long reinforced composites based on the phase field approach of fracture combined with the cohesive zone model, International Journal of Fracture (under revision) (2019).
[45] A. Puck, H. Schürmann, Failure analysis of frp laminates by means of physically based phenomenological models, Composites Science and Technology 62 (12) (2002) 1633 – 1662. doi:https://doi.org/10.1016/S0266-3538(01)00208-1.
URL http://www.sciencedirect.com/science/article/pii/S0266353801002081
[46] M. Eftekhari, A. Fatemi, Tensile behaviour of thermoplastic composites including temperature, moisture, and hygrothermal effects, Polymer Testing 51 (2016) 151–164.
[47] M. Vogler, F. Andrade, J.Schöpfer, S. Kolling, R. Rolfes, A novel transversely-isotropic 3d elastic-viscoplastic constitutive law for modeling fiber matrix composites, in: 8th European LS-DYNA users conference, Strasbourg, France,, 2011.
[48] I. Vladimirov, S. Reese, Production simulation by means of a structure tensor based framework of anisotropic plasticity, Proceedings in Applied Mathematics and Mechanics 12 (2012) 823–826.
[49] P. Papadopoulos, J. Lu, On the formulation and numerical solution of problems in anisotropic finite plasticity, Computer Methods in Applied Mechanics and Engineering 190 (2001) 4889–4910.
[50] A. Dean, S. Sahraee, K. Ozenc, J. Reinoso, R. Rolfes, M. Kaliske, A thermodynamically consistent framework to couple damage and plasticity microplane-based formulations for fracture modeling: development and algorithmic treatment, International Journal of Fracture 203 (2016) 115–134. doi:10.1007/s10704-016-0131-9.
[51] W. Wagner, C. Balzani, Prediction of the postbuckling response of composite airframe panels including ply failure, Engineering Fracture Mechanics 77 (18) (2010) 3648 – 3657, computational Mechanics in Fracture and Damage: A Special Issue in Honor of Prof. Gross. doi:https://doi.org/10.1016/j.engfracmech.2010.05.009.
URL http://www.sciencedirect.com/science/article/pii/S0013794410002407

[52] J.-Y. Wu, T. Mandal, V. P. Nguyen, A phase-field regularized cohesive zone model for hydrogen assisted cracking, Computer Methods in Applied Mechanics and Engineering 358 (2019) 112614. doi:10.1016/j.cma.2019.112614.
[53] H. M. Deuschle, B.-H. Kröplin, Finite element implementation of puck's failure theory for fibre-reinforced composites under three-dimensional stress, Journal of Composite Materials 46 (19-20) (2012) 2485–2513. doi:10.1177/0021998312451480.
[54] A. Dean, J. Reinoso, N. Jha, E. Mahdi, R. Rolfes, A phase field approach for ductile fracture of short fibre reinforced composites, Theoretical and Applied Fracture Mechanics 106 (2020) 102495. doi:https://doi.org/10.1016/j.tafmec.2020.102495.
URL http://www.sciencedirect.com/science/article/pii/S0167844219306536
[55] J. Fang, C. Wu, T. Rabczuk, C. Wu, C. Ma, G. Sun, Q. Li, Phase field fracture in elasto-plastic solids: Abaqus implementation and case studies, Theoretical and Applied Fracture Mechanics 103 (2019) 102252.
[56] P. K. Kristensen, E. Martínez-Pañeda, Phase field fracture modelling using quasi-newton methods and a new adaptive step scheme, Theoretical and Applied Fracture Mechanics (2019) 102446doi:https://doi.org/10.1016/j.tafmec.2019.102446.
URL http://www.sciencedirect.com/science/article/pii/S0167844219305580
[57] J.-Y. Wu, Y. Huang, Comprehensive implementations of phase-field damage models in abaqus, Theoretical and Applied Fracture Mechanics 106 (2020) 102440. doi:https://doi.org/10.1016/j.tafmec.2019.102440.
URL http://www.sciencedirect.com/science/article/pii/S0167844219306871
[58] A. S. Kaddour, M. Hinton, Input data for test cases used in benchmarking triaxial failure theories of composites, Journal of Composite Materials 46 (2012) 2295–2312. doi:10.1177/0021998312449886.
[59] C. Gerendt, A. Dean, T. Mahrhol, R. Rolfes, On the progressive failure simulation and experimental validation of fiber metal laminate bolted joints, Composite Structures 229 (2019) 111368. doi:10.1016/j.compstruct.2019.111368.
[60] A. Dean, N. Safdar, R. Rolfes, A co-rotational based anisotropic elasto–plastic model for geometrically non-linear analysis of fibre reinforced polymer composites: Formulation and finite element implementation, Materials 12 (11) (2019). doi:10.3390/ma12111816.
URL https://www.mdpi.com/1996-1944/12/11/1816
[61] P. Camanho, C. Dávila, S. Pinho, L. Iannucci, P. Robinson, Prediction of in situ strengths and matrix cracking in composites under transverse tension and in-plane shear, Composites Part A: Applied Science and Manufacturing 37 (2006) 165–176. doi:10.1016/j.compositesa.2005.04.023.
[62] H. Krüger, Ein physikalisch basiertes ermüdungsschädigungsmodell zur degradationsberechnung von faser-kunststoff-verbunden, Doctoral degree, dissertation thesis, Leibniz Universität Hannover (2012).
[63] M. Brod, G. Just, A. Dean, E. Jansen, I. Koch, R. Rolfes, M. Gude, Numerical modelling and simulation of fatigue damage in carbon fibre reinforced plastics at different stress ratios, Thin-Walled Structures 139 (2019) 219–231. doi:10.1016/j.tws.2019.03.005.
[64] B. Arash, W. Exner, R. Rolfes, A viscoelastic damage model for nanoparticle/epoxy nanocomposites at finite strain: A multiscale approach, Journal of the Mechanics and Physics of Solids 128 (2019) 162–180. doi:10.1016/j.jmps.2019.04.004.
[65] B. Arash, W. Exner, R. Rolfes, Viscoelastic damage behavior of fiber reinforced nanoparticle-filled epoxy nanocomposites: Multiscale modeling and experimental validation, Composites Part B Engineering 174 (107005) (2019). doi:10.1016/j.compositesb.2019.107005.